Tensile behavior of rebar-reinforced coarse aggregate ultra-high performance concrete (R-CA-UHPC) members

Experiments and restrained shrinkage creep effect

Shi, Zhanchong; Liang, Minfei; Su, Qingtian; Kanstad, Terje; Ferrara, Liberato

DOI
10.1016/j.cemconcomp.2024.105574

Publication date
2024

Document Version
Final published version

Published in
Cement and Concrete Composites

Citation (APA)
Shi, Z., Liang, M., Su, Q., Kanstad, T., & Ferrara, L. (2024). Tensile behavior of rebar-reinforced coarse aggregate ultra-high performance concrete (R-CA-UHPC) members: Experiments and restrained shrinkage creep effect. *Cement and Concrete Composites*, *151*, Article 105574. https://doi.org/10.1016/j.cemconcomp.2024.105574

Cement and Concrete Composites 151 (2024) 105574

Contents lists available at ScienceDirect

Cement and Concrete Composites

journal homepage: www.elsevier.com/locate/cemconcomp

Tensile behavior of rebar-reinforced coarse aggregate ultra-high performance concrete (R-CA-UHPC) members: Experiments and restrained shrinkage creep effect

Zhanchong Shi [a,b], Minfei Liang [c], Qingtian Su [a,d,*], Terje Kanstad [b], Liberato Ferrara [e]

[a] Department of Bridge Engineering, Tongji University, Shanghai, 200092, China
[b] Department of Structural Engineering, Norwegian University of Science and Technology, Richard Birkelandsvei 1A, 7034, Trondheim, Norway
[c] Microlab, Delft University of Technology, 2628 CN, Delft, the Netherlands
[d] Shanghai Engineering Research Center of High Performance Composite Bridges, Shanghai, 200092, China
[e] Department of Civil and Environmental Engineering, Politecnico di Milano, Piazza Leonardo DaVinci 32, 20133, Milan, Italy

ARTICLE INFO

Keywords:
CA-UHPC members
Axial tensile response
Restrained shrinkage
Tensile creep
First cracking strength

ABSTRACT

Rebar-reinforced coarse aggregate ultra-high-performance concrete (R-CA-UHPC) has been used in the construction of new structures and strengthening of deteriorated aged infrastructures, and it inevitably sustains tension. To study the tensile behavior of R-CA-UHPC members, axial tensile tests for dog-bone-shaped specimens were designed and conducted. The investigated variables included reinforcement ratio in terms of rebar quantity/diameter, and concrete type (CA-UHPC vs. normal concrete). The test results showed that the improved rebar/CA-UHPC bond property prevents the emergence of splitting cracks, but intensifies the crack localization for CA-UHPC and strain concentration for rebar after yielding. Moreover, the restrained effect of rebar on free shrinkage of CA-UHPC leads to a decrease in the first cracking strength for R-CA-UHPC members. Based on the established development functions of elastic modulus, autogenous shrinkage, and tensile creep for CA-UHPC, the restrained effect was quantified according to Dischinger's-differential-equation-based theoretical analysis. Finally, the models to predict the first cracking stresses/strains and the yielding loads of the R-CA-UHPC members were developed and validated.

1. Introduction

Ultra-High-Performance Concrete (UHPC), as a nowadays "state-of-art" category of fiber-reinforced cementitious composites, features superior mechanical and durability performances, which are typically characterized by Ref. [1]: (1) compressive strength higher than 120 MPa; (2) elastic modulus greater than 40 GPa; (3) sustained post-cracking tensile strength larger than 5 MPa; and (4) a disconnected pore structure that significantly reduces permeability and thus enhances durability. UHPC is expected to be applied in the construction of new structures, characterized by longer spans, higher rise, shallower depth, and smaller cross-sectional area, and has been used in rehabilitation and strengthening of aged infrastructures, such as deteriorated concrete slabs and beams [2–5] and fatigue-cracked orthotropic steel bridge decks [6–8]. Whereas, the use of an extremely low water-binder (w/b) ratio of less than 0.2 and a substantial amount of binder of typically 800–1200 kg/m^3 make UHPC have a significantly higher autogenous shrinkage compared to normal concrete and high-performance concrete [9]. To address this issue, one solution is to introduce coarse aggregate (CA) to partially replace binders in UHPC, obtaining what is also known as coarse aggregate UHPC (CA-UHPC), because the stiff and high elastic modulus of CA contributes to restraining shrinkage deformation of UHPC [10]. It has been demonstrated that, with the appropriate addition of coarse aggregates, CA-UHPC features higher compressive strength and elastic modulus and a slight decrease in tensile capacity and post-cracking toughness, as compared with "conventional" UHPC mixes (with the same paste ratio) with only (very) fine aggregates [11,12].

Though exhibiting a slightly deteriorated tensile behavior, CA-UHPC is expected to be co-reinforced with steel rebars and employed in tension zones of concrete structures. Current research on the tensile properties of CA-UHPC mainly focuses on the material level. Shi et al. [13] have

* Corresponding author. 1239 Siping Road, Tongji University, Shanghai, 200092, China.
E-mail address: sqt@tongji.edu.cn (Q. Su).

https://doi.org/10.1016/j.cemconcomp.2024.105574
Received 1 February 2024; Received in revised form 30 April 2024; Accepted 1 May 2024
Available online 4 May 2024

developed the tensile constitutive model and tensile damage evolution law for CA-UHPC based on quasi-static uniaxial tensile tests, demonstrating that CA-UHPC exhibits approximately linear-elastic response up to tensile strength followed by tension softening. Li et al. [14] conducted uniaxial tensile fatigue test and 3D numerical simulation for CA-UHPC with different volume additions of CA, revealing that CA weakens the fatigue deformation capacity and accelerates the initiation of tensile fatigue damage at the early stage, resulting in premature fatigue failure. Cheng [15] established the flexural tensile fatigue *S–N* curves with different survival probabilities for CA-UHPC based on four-point bending cyclic tests. As for the tensile behavior of CA-UHPC at the structural level, quasi-static flexural [16,17] as well as the fatigue flexural tests [18,19] have been performed on rebar-reinforced CA-UHPC (R-CA-UHPC) bridge decks to reveal the flexural response and fatigue resistance. However, to the authors' knowledge, there is currently no study on the axial tensile behavior of R-CA-UHPC elements at the member level. The axial tensile behavior of R-CA-UHPC members better reflects the synergistic tensile response of rebar and CA-UHPC compared to the flexural performance of R-CA-UHPC members or structures.

Recent studies on axial tensile behavior of rebar-reinforced UHPC (R–UHPC) members mainly employed UHPC without CA, and focused on the influences of material parameters, including reinforcement ratio, rebar type (plain and ribbed rebars, normal and high strength rebars), fiber volume fraction, fiber distribution, and fiber chemical treatment, on the tensile response [20–31]. Overall, the consistent conclusion that UHPC contributes a substantial tensile capacity to the member response even after rebar yields, can be drawn. However, only Yuan [23], Bian et al. [26,28], and Guo et al. [27] reported that the first cracking strength of the R–UHPC member is significantly lower than the elastic tensile strength of the "parent" UHPC material, and this difference increases with the growing reinforcement ratio. This can be interpreted by the restrained effect of rebar on the free shrinkage of UHPC.

Past research regarding the cracking of restrained concrete [32,33], including internal restraint (such as rebar) as well as external restraint (such as boundary conditions), has demonstrated that restrained shrinkage leads to tensile stress which may result in even premature cracking in concrete. Whereas the tensile creep partially counteracts the tensile stress in concrete through a stress relaxation mechanism. Whether the significantly high autogenous shrinkage of UHPC will induce, if restrained, tensile stresses even more prominent in R–UHPC members before external loading deserves to be investigated. What's more, the influence of the restrained shrinkage on the first cracking strength of R–UHPC members hasn't been quantified. Moreover, whether the axile tensile response of R–UHPC members is suitable for R-CA-UHPC members is thus to be investigated further.

Consequently, this study mainly focuses on the axial tensile behavior of R-CA-UHPC members based on the quasi-static axial tensile test, and the influence of reinforcement ratios and concrete types was investigated. This paper compares the global tensile response, cracking patterns, and ultimate failure modes between R-CA-UHPC and rebar-reinforced normal concrete (R–NC) members. The influence of restrained shrinkage and tensile creep on the restrained tensile stress at the curing stage was quantified according to Dischinger-differential-equation-based theoretical analysis. On this basis, concepts of restraint degree and free degree were proposed to characterize the restrained shrinkage creep effect, and prediction models for the first cracking strength/strain and the yielding load for R-CA-UHPC members were developed and validated.

2. Research significance

This study enhances a comprehensive understanding of the synergistic tensile performance of CA-UHPC and steel rebar, providing deeper insights into the tensile characterizations, cracking formations, and restrained shrinkage-induced mechanical responses for R-CA-UHPC elements. By bridging the gap between material science and engineering practice, this advancement will facilitate the design application of CA-UHPC material in civil infrastructures.

3. Experimental program

3.1. Specimen design and production

Dog-bone-shaped reinforced concrete specimens, as shown in Fig. 1, were designed to conduct the axial tensile test. The specimens were 100 mm thick and 560 mm long, with a cross-section 50 mm wide in the central part, which tapered to 100 mm at the edges. To quantify the synergistic tensile property of rebar and CA-UHPC elements, and to compare the difference in the tensile response between R-CA-UHPC members and rebar-reinforced normal concrete (R–NC) members, three parameters were assumed as experimental variables: (a) the reinforcement ratio, equal to 1.6 %, 3.2 %, and 5.0 %, obtained with one, two or three 10 mm diameter bars respectively; (b) the bar diameter d_s, equal to 10 mm, 12 mm, 14 mm, and 16 mm with one single rebar, corresponding to reinforcement ratio of 1.6 %, 2.3 %, 3.2 %, and 4.2 %, respectively, (c) concrete type, either CA-UHPC or NC. Table 1 provides a synopsis of the experimental variables and program.

For each combination of experimental variables, five nominally identical samples numbered SN-1 to SN-5 were produced. Seven strain gauges (8 mm long and 5 mm wide) with uniform spacing of 40 mm, shown in Fig. 1(a) and (e), were attached to the rebar surface (embedded in concrete) only for specimens SN-3 and SN-4 to measure the strain distribution along the bars; it is worth remarking that the first cracking load may be affected by the increased reduction of cross-section induced by the wires of strain gauges. Only one rebar was provided with strain gauges for the specimen with two rebars, while only the middle rebar was equipped with strain gauges for the specimen with three rebars.

The casting process of the specimens was as follows: first, the rebars were fixed at the specimen mold, shown in Fig. 1(e), then the fresh concrete mixture was cast into the mold which was vibrated for 2–3 min afterward. The specimens were covered with plastic film immediately after vibration to prevent moisture evaporation. Finally, the specimens were demolded 24 h (at room temperature of 20 ± 2 °C) after casting and cured for 28 days at the standard curing room with a temperature of 20 ± 2 °C and a relative humidity of 95 %.

3.2. Test setup and loading protocol

Fig. 1(f) shows the axial tensile test setup. A servo-hydraulic testing machine was used to enforce direct tensile load to the specimen under constant displacement control at a rate of 0.4 mm/min. According to preliminary experimental measurement, the displacement of the rigid crossbeam of the test setup was close to the measured elongation. Therefore, the machine stroke was used for control. Two extensometers with an accuracy of 0.001 mm were attached to the central part (longitudinal direction) of the specimen over a gauge length of 200 mm to measure the axial elongation. The opening of the cracks within the gauge length was captured by a crack observation instrument with an accuracy of 0.01 mm. In addition, the strain evolution along the rebar was recorded by strain gauges and the DH3816 N static data acquisition instrument. As shown in Fig. 2, specimens SN-1∼SN-4 were loaded to a maximum elongation of 6.5 mm (half of the steel fiber length l_f, $l_f = 13$ mm) and unloaded, while specimens SN-5 were loaded to the ultimate failure.

3.3. Material properties characterization

3.3.1. Concrete

The two concrete materials used were commercial ones. CA-UHPC was composed of reactive powder, river sand, basalt aggregate (maximum particle size less than 8 mm), superplasticizer, water, and

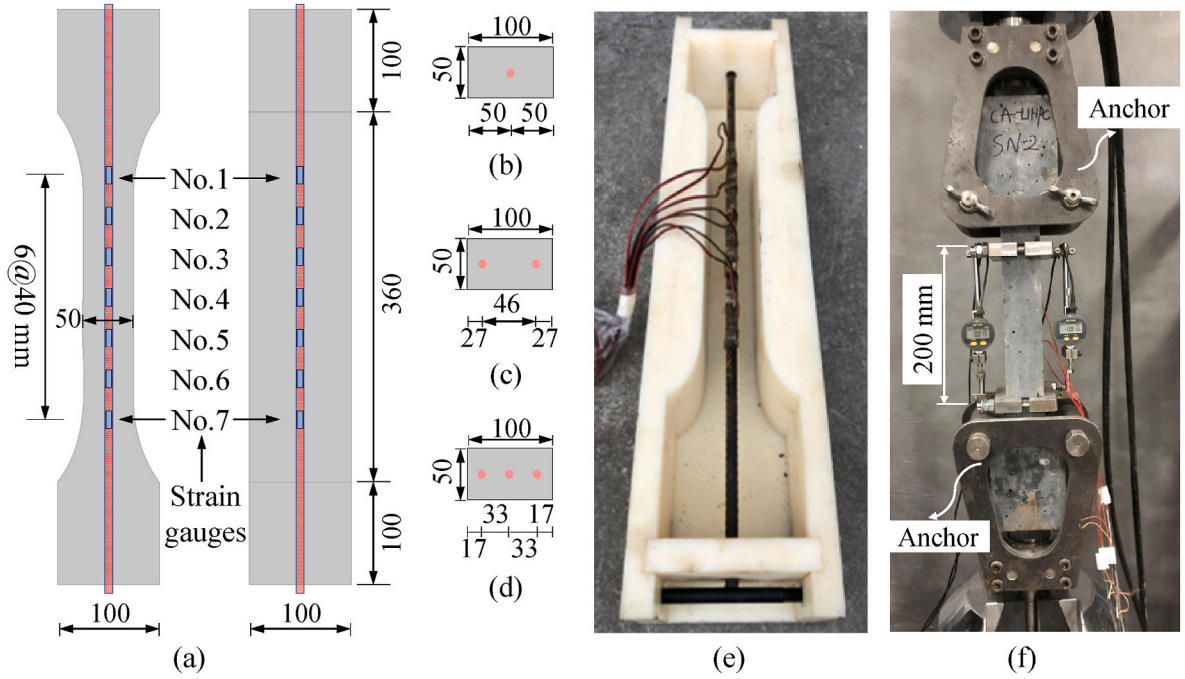

Fig. 1. Specimen details (unit: mm): (a) sample size and arrangement of rebar strain gauges; (b) cross section with single rebar; (c) cross section with two rebars; (d) cross section with three rebars; (e) specimen mold; (f) axial tensile test setup.

Table 1
Specimen details of reinforced concrete.

Rebar configuration	ρ_s	c [mm]	Specimen number	Concrete type
d_s10	1.6 %	20	SN-1~SN-5	CA-UHPC
2d_s10	3.2 %	20	SN-1~SN-5	CA-UHPC
3d_s10	5.0 %	12	SN-1~SN-5	CA-UHPC
d_s12	2.3 %	19	SN-1~SN-5	CA-UHPC
d_s14	3.2 %	18	SN-1~SN-5	CA-UHPC
d_s16	4.2 %	17	SN-1~SN-5	CA-UHPC
d_s12	2.3 %	19	SN-1~SN-5	NC

Notes: ρ_s, c denote reinforcement ratio and minimum concrete cover, respectively.

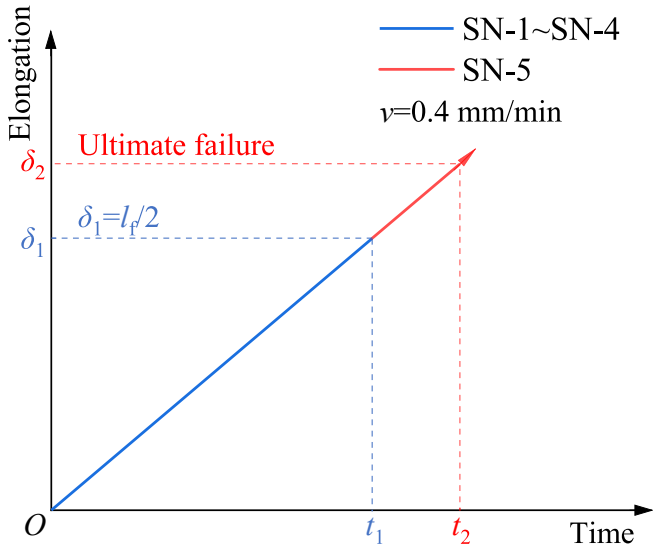

Fig. 2. Loading protocol.

steel fibers, as shown in Fig. 3 and Table 2. The steel fibers were a fiber cocktail containing straight fibers (length of 13 mm and diameter of 0.2 mm) as well as hooked-end fibers (length of 20 mm and diameter of 0.25 mm). The total fiber dosage was 2.5 % by volume (1 % of straight fibers and 1.5 % of hooked-end ones). The elastic modulus and tensile strength of the two steel fibers were 200 GPa and 2850 MPa, respectively. NC did not contain steel fibers, and the composition of NC is listed in Table 3.

Axial tensile tests were conducted on the investigated CA-UHPC and NC (unreinforced) using the same dog-bone-shaped specimens as for the R-CA-UHPC/RC to identify the tensile constitutive relationship. Referring to Chinese Standard CECS13 [34], 100 mm × 100 mm × 300 mm prisms for CA-UHPC and 150 mm × 150 mm × 300 mm ones for NC, were used to obtain the elastic modulus and axial compressive strength. Each test was performed on three nominally identical specimens, and the corresponding average values and standard deviations are summarized in Table 4. It should be noted that the casting process and curing condition of the material property test specimens were the same as the reinforced concrete specimens mentioned above.

According to the axial tensile results and the author's previous work [13], the direct tensile behavior of the CA-UHPC is characterized by an approximately linear stress-strain relation up to the peak stress (tensile strength) and the post-peak tensile softening response, which is mainly induced by the weak zone at the coarse-aggregate/matrix interface. Therefore, CA-UHPC was considered the strain-softening type according to the axial tensile response. The tensile constitutive model of CA-UHPC was established, plotted in Fig. 4, and the corresponding characteristic parameters f_{ct}, f_{ctr}, ε_{ctr}, and $\varepsilon_{ct,max}$ are listed in Table 4. As shown in Fig. 4, the softening branch is divided into the multi-cracking stage (corresponding to branch AB) and the localized-cracking stage (corresponding to branch BC).

3.3.2. Rebar

The steel rebar used was HRB400 which is mostly used in concrete bridges in China. Axial tensile tests on rebar samples (three per diameter) were performed according to the Chinese standard [35]. The obtained tensile stress-strain curves for the rebar are shown in Fig. 5(a)~(d). A simplified bilinear constitutive model (Fig. 5(e)) was developed based on the tensile stress-strain curves, and the characteristic

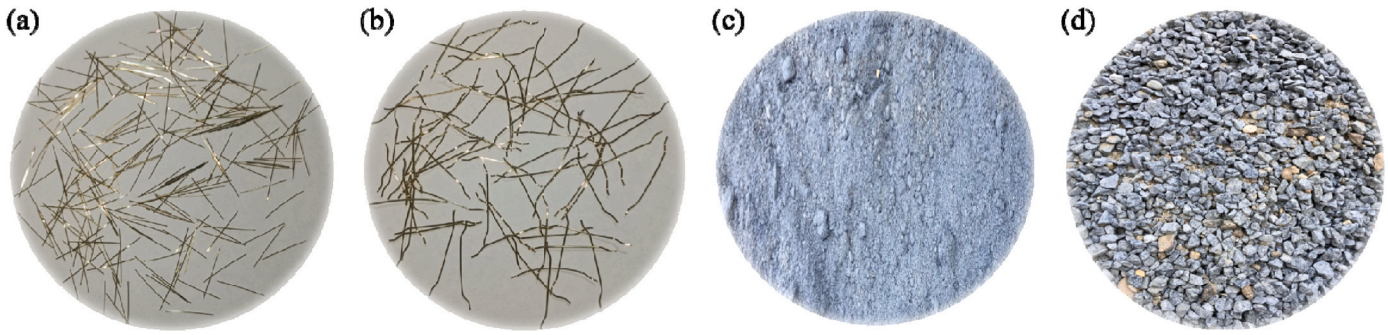

Fig. 3. Main compositions of CA-UHPC: (a) straight steel fibers; (b) hooked-end steel fibers; (c) reactive powder; (d) basalt aggregates.

Table 2
Material compositions of 1 m^3 CA-UHPC (unit: kg).

Reactive powder	Sand	Basalt aggregates	Steel fibers		Superplasticizer	Water
			straight	hooked		
1173	616	472	89	109	25.7	138

Table 3
Material compositions of 1 m^3 NC (unit: kg).

Gravel	Sand	Cement	Water reducer	Water
1080	780	450	4.5	154

Table 4
Basic mechanical properties of investigated concretes.

Concrete	E_c [MPa]	f_c [MPa]	f_{ct} [MPa]	f_{ctr} [MPa]	ε_{ctr} [$\times 10^{-6}$]	$\varepsilon_{ct,max}$ [$\times 10^{-6}$]
CA-UHPC	52000 ± 6538	128 ± 10	7.83 ± 0.78	6.47 ± 0.84	2500	32500
NC	36633 ± 3296	49 ± 5	2.59 ± 0.28	–	–	–

Notes: E_c and f_c denote elastic modulus and compressive strength, respectively. f_{ct}, f_{ctr}, ε_{ctr}, and $\varepsilon_{ct,max}$ are the tensile strength, post-peak residual tensile strength, post-peak residual tensile strain, and maximum tensile strain, respectively.

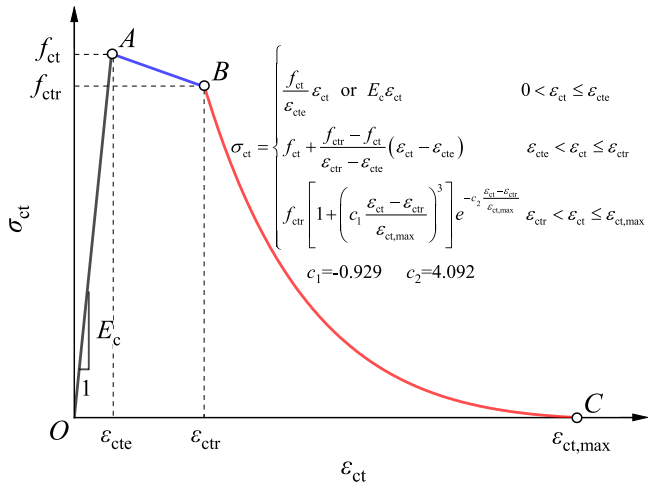

Fig. 4. Tensile constitutive model of CA-UHPC [13].

parameters of the model are presented in Table 5. These parameter values represented the average values obtained from the successfully tested specimens in which fracture occurred within the gauge length of the extensometer.

4. Test results and analysis

4.1. Axial load-member strain response

4.1.1. General axial tensile response

The axial load vs. average member strain response of the tested R-CA-UHPC and R–NC specimens is plotted in Fig. 6. The average member strain was obtained by dividing the mean value of the elongations measured through the two extensometers by the gauge length of 200 mm. Fig. 6 also compares the axial tensile response between the reinforced concrete member and the bare rebar, in which the bare rebar response was obtained using the bilinear constitutive model developed above.

As shown, the axial tensile response curve of the R–NC specimen is almost the same as that of the bare rebar, indicating that the NC provides limited tensile capacity to the R–NC members. By contrast, the axial tensile response curve of the R-CA-UHPC specimen lies evidently above the bare rebar curve, and the significant gap between the two curves stands for the CA-UHPC's contribution to the tensile bearing capacity of the R-CA-UHPC members. Specimens SN-1 and SN-2 always have excellent repeatability, while the tensile responses of specimens SN-3 and SN-4, in most cases (for d_s10, 2d_s10, 3d_s10, and d_s12), are located below that of specimens SN-1 and SN-2, which can probably be due to some disturbance effects of the strain gauges, also on the flow of the CA-UHPC and hence on fiber dispersion. Therefore, the following analysis of axial load vs. average member strain will be mainly based on the test results of specimens SN-1 and SN-2.

The representative axial tensile response, as from the tested R–NC/CA-UHPC members, is plotted in Fig. 7. The first cracking point (ε_{cr}, P_{cr}) was determined by the initial shifting from the linear-elastic tensile response curve. The yielding point (ε_y, P_y) was obtained when the average member strain reached the yielding strain of the rebar listed in Table 5. The peak point (ε_m, P_m) was achieved as the axial load reached the maximum value. The fracture point (ε_f, P_f) indicated the moment the rebar was ruptured, and this point was identified based on the ultimate axial tensile response of specimen SN-5.

As shown in Fig. 7, the axial tensile response of R–NC members could be divided into three phases.

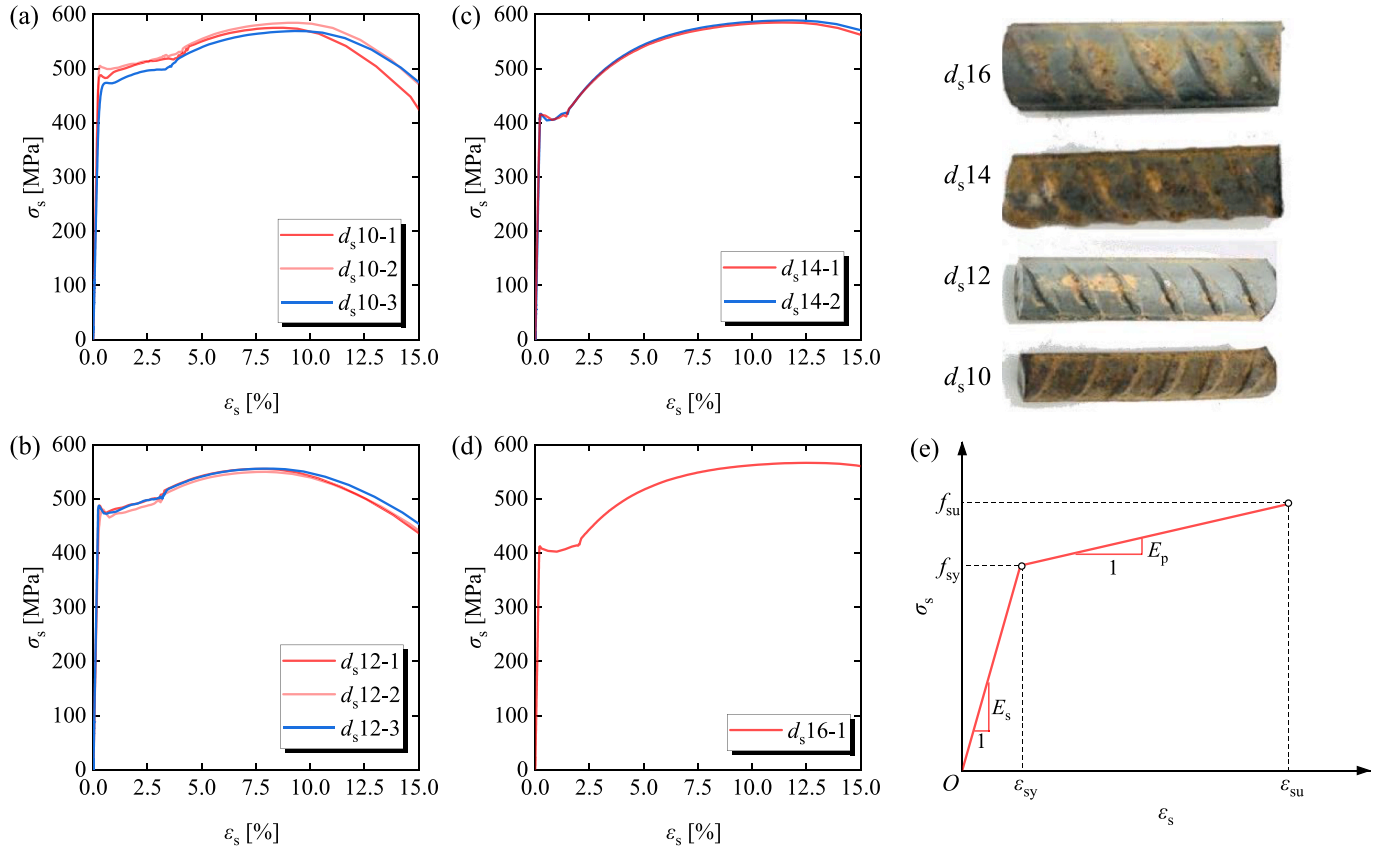

Fig. 5. Tensile stress-strain curves of the rebar: (a) d_s10 mm; (b) d_s12 mm; (c) d_s14 mm; (d) d_s16 mm; (e) simplified bilinear constitutive model.

Table 5
Characteristic parameters of the bilinear constitutive model for the steel rebar.

d_s [mm]	f_{sy} [MPa]	f_{su} [MPa]	εsy [× 10^{-6}]	εsu [× 10^{-6}]	E_s [MPa]	E_p [MPa]
10	488	577	2438	90042	200187	1010
12	470	554	2382	77811	197439	1103
14	406	587	2104	116164	192978	1587
16	407	566	1958	124925	207880	1296

Notes: f_{sy}, f_{su}, ε_{sy}, ε_{su}, E_s, and E_p denote the yielding strength, tensile strength, yielding strain, tensile strain corresponding to the tensile strength, elastic modulus, and plastic modulus, respectively.

Phase I: linear-elastic phase, featured by the linear axial load-average member strain relation until NC reaches its tensile strength. The first cracking of NC marks the end of this Phase.
Phase II: stabilized cracking phase. At this phase, the concrete at the cracked location enters its softening stage, and the tensile force is transferred to the neighboring concrete that has not yet cracked through the bond interaction between rebar and concrete. New transverse cracks continue to appear in the concrete and develop into main cracks with a saturated distribution until the rebar yields.
Phase III: yielding phase, characterized by the pronounced yielding plateau of the tensile response curve; the formation of longitudinal splitting cracks along the rebar has been observed in this stage, as a result of the failure of the bond mechanism, which can be reflected by the unevenness at the yielding plateau shown in Fig. 7(a). The splitting cracks continue to propagate until they intersect with the transverse cracks, splitting the R–NC members into several sub-components bounded by longitudinal and transverse cracks, presenting the ultimate failure mode of "shattering to pieces", shown in sec. 4.4 below. It is noteworthy that only rebar bears tension at the yielding phase.

By contrast, the axial tensile response of the R-CA-UHPC members could be divided into four phases, including the linear-elastic phase, stabilized cracking phase, yielding phase, and rebar fracture phase. The first three phases of the R-CA-UHPC members are generally the same as the R–NC members, the differences are:

(a) The CA-UHPC at the cracked sections can still bear tension due to the fiber bridging effect and the pull-out effect of debonding between the steel fibers and the matrix.
(b) Although new transverse cracks continue to appear for the R-CA-UHPC members at the stabilized cracking phase (phase II in Fig. 7 (b), corresponding to the multi-cracking softening stage of CA-UHPC material as described in sec.3.3.1), only one transverse crack develops into a localized main crack once reaching yielding (phases III and IV in Fig. 7(b), corresponding to the localized-cracking softening stage of CA-UHPC material as described in sec.3.3.1). Consequently, the rest transverse cracks are gradually closed due to the squeezing effect caused by the continuous opening of the localized crack.
(c) No splitting cracks initiate for the R-CA-UHPC members at the yielding phase, indicating that the higher tensile strength of CA-UHPC suppresses the occurrence of splitting cracking. Moreover, the axial load continues to increase at this phase without a yielding plateau, suggesting that the excellent interface bond property between rebar and CA-UHPC ensures the synergy to withstand tension even after crack localization.
(d) After crossing the peak point, as the main crack continues to expand, the rebar at the main crack location is broken while the

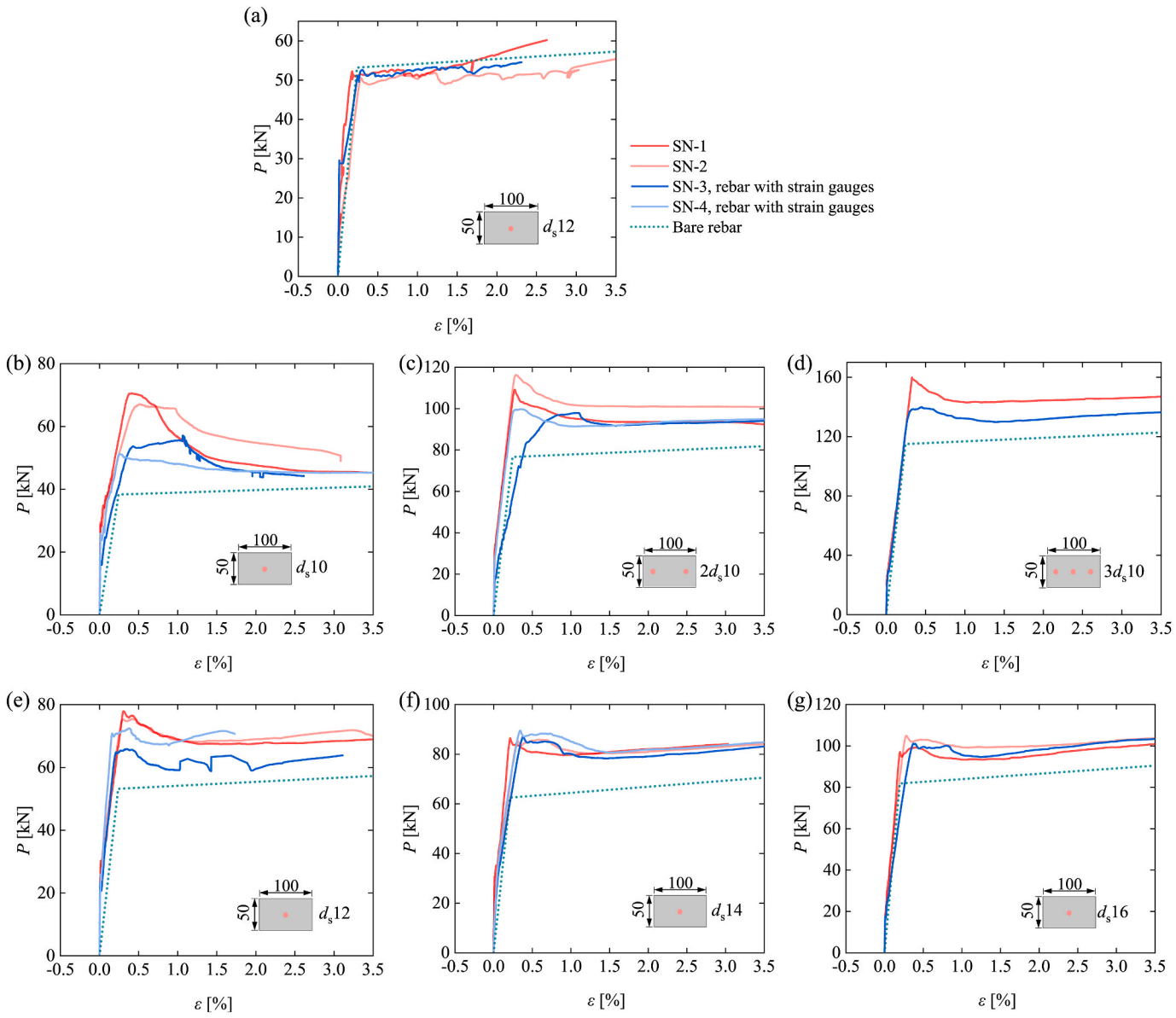

Fig. 6. Axial load-average member strain response of reinforced concrete members: (a) R–NC; (b) R-CA-UHPC, d_s10; (c) R-CA-UHPC, $2d_s$10; (d) R-CA-UHPC, $3d_s$10; (e) R-CA-UHPC, d_s12; (f) R-CA-UHPC, d_s14; (g) R-CA-UHPC, d_s16.

two ends of the rebar are firmly anchored in CA-UHPC, as shown in sec.4.4.

4.1.2. *Influence of investigated parameters*

The influence of investigated parameters, i.e., rebar quantity, rebar diameter, and concrete type, on the axial tensile response of R-CA-UHPC members is shown in Fig. 8. It is obvious that the post-peak tensile capacity exhibited a linear increment with the rebar quanty. As the rebar quanty grows from 0 to 1, 2, and 3, the increases of post-peak tensile capacity were 44 kN, 46 kN, and 50 kN, respectively. The increases were approximately equal to the yield-bearing capacity $f_{sy}A_s$ (A_s is the cross-sectional area of a single bar) of a single rebar. As plotted in sec.4.4, because all the R-CA-UHPC members with different rebar quantities exhibit crack localization at the post-yielding stages, the post-peak tensile capacity differences are determined by the rebar quantities.

For rebar diameter, as it increased from 10 mm to 16 mm (the corresponding reinforcement ratio increased from 1.6 % to 4.2 %), the post-peak tensile capacity also showed an increasing trend, and the increase of the post-peak residual bearing capacity was the difference between the yield-bearing capacity of the single bar ($\Delta f_{sy}\Delta A_s$). This phenomenon is induced by the post-yielding crack localization for the R-CA-UHPC members with different rebar diameter, as plotted in sec.4.4. As for concrete type, CA-UHPC exhibited obvious advantages over NC in synergistic tensile properties with rebar, which is not only reflected in the higher tensile strength and excellent post-cracking residual tensile strength CA-UHPC, but also in the excellent rebar/concrete interface bond properties. Due to the enhanced interface bond strength, no pronounced splitting cracks emerged at the R-CA-UHPC members, while the R–NC members were prone to severe splitting cracking, as shown in the crack pattern comparison in sec.4.4.

4.2. *Rebar strain distribution*

Fig. 9 shows the rebar strain distribution of R-CA-UHPC members. In general, the strain distribution along rebar length was not uniform, which could be explained by the stress concentration of the rebar induced by the crack localization of CA-UHPC. The strain gauges located around the main crack presented relatively larger strain values, which

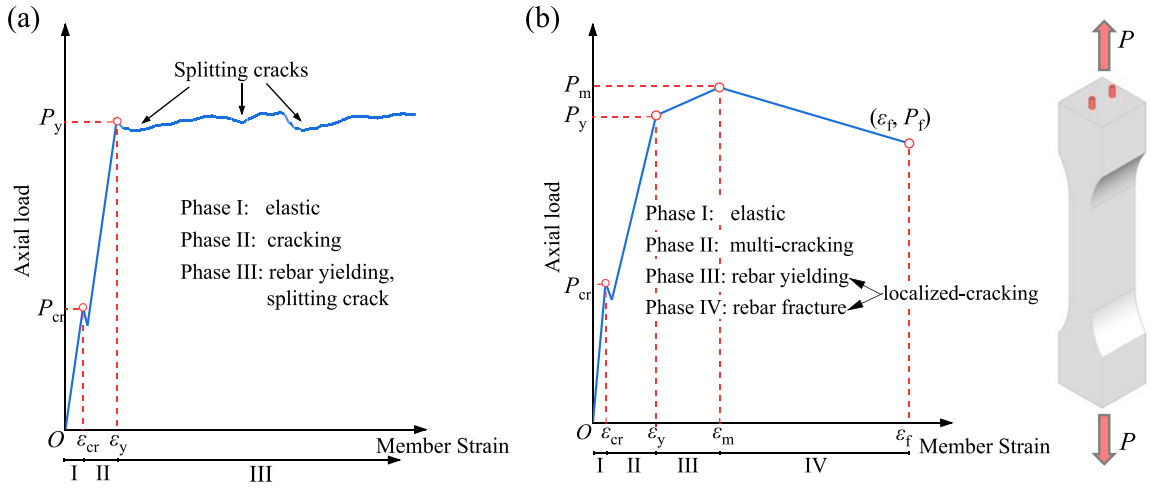

Fig. 7. Schematic representative of the axial tensile response of reinforced concrete members: (a) R–NC; (b) R-CA-UHPC.

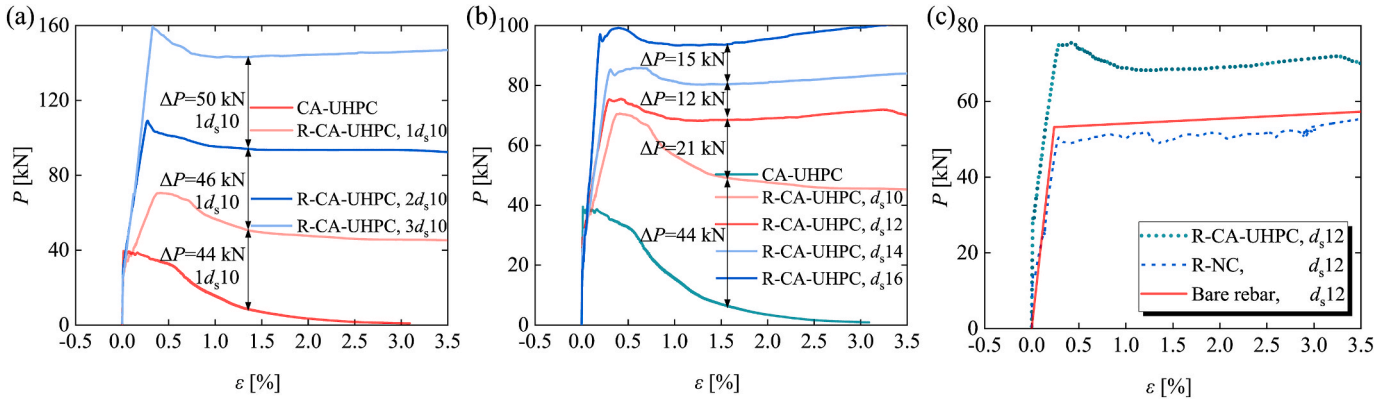

Fig. 8. Analysis of investigated parameters: (a) rebar quantity; (b) rebar diameter; (c) concrete type.

were induced by the transfer of tensile force from CA-UHPC to rebar at the crack. Especially, strain concentration and early strain hardening of rebar developed once crack localization of CA-UHPC occurred, as the measured strain by rebar strain gauges located around the main crack was higher than the average member strain after member strain approached approximately the yielding strain (ε = 0.2 %).

4.3. Distinctive loads and strains

Table 6 summarizes the values of the distinctive loads and strains of R-CA-UHPC members. The theoretical first cracking strain $\varepsilon_{cr,The}$ is the elastic limit tensile strain ε_{cte} based on the tensile constitutive model of CA-UHPC (see Fig. 4), $\varepsilon_{cr,The} = \varepsilon_{cte} = f_{ct}/E_c$. Accordingly, the theoretical first cracking load $P_{cr,The}$ was obtained according to $P_{cr,The}=(E_cA_c + E_sA_s)\varepsilon_{cr,The}$, where A_c is the net cross-sectional area. The theoretical yielding load was calculated according to $P_{y,The} = f_{sy}A_s+\sigma_{ct}A_c$, where σ_{ct} is the tensile strength of CA-UHPC as average member strain reaching ε_y based on the tensile constitutive model of CA-UHPC, shown in Fig. 4.

Fig. 10 compares the theoretical first cracking loads and strains with the experimentally measured ones. It was obvious that the test values were lower than the theoretical values, neglecting the influence of matrix inhomogeneity of CA-UHPC and fiber distribution non-uniformity caused by reinforcement. Moreover, the differences between the test and theory increased significantly with the increase of the reinforcement ratio, the differences in first cracking strains ranged from 26 % to 48 % as the reinforcement ratio changed from 1.6 % to 5.0 %, while the differences in the first cracking loads varied from 30 % to 57 %. The pronounced decrease of cracking loads and strains may be induced by the emergence of pre-tension in CA-UHPC at the curing stage, where the free shrinkage of CA-UHPC was restrained by the rebar. The related mechanism and quantification of the effect will be explained in detail in the next section.

Fig. 11(a) shows the comparison between the theoretical and experimental yielding loads. In general, the tested yielding load was 17 % lower than the theoretical one. This also could be interpreted by the restrained effect of rebar on the free shrinkage of CA-UHPC, which generated pre-compressive stress in the rebar prior to the external load being applied. The experimental yielding loads were obtained as the average member stain reaching ε_y. At the moment, the rebar actually did not yield due to overcoming the pre-compression first. Fig. 11(b) compares the test yielding and peak loads. As shown, the yielding loads were relatively close to the peak load, and the mean yielding load is 86 % of the mean peak load. The same experimental phenomenon can be found in existing studies [24,25,27] on the tensile property of rebar-reinforced UHPC (without coarse aggregate) members.

4.4. Crack distribution and ultimate failure modes

No visible cracks were observed for all the specimens prior to loading, indicating that the restrained effect of the rebar on the concrete at the curing stage did not lead to the cracking of concrete at an early age. Fig. 12 shows the typical crack distribution of the tested reinforced concrete members at the maximum elongation equal to half the steel fiber length. The R–NC members presented uniformly distributed and

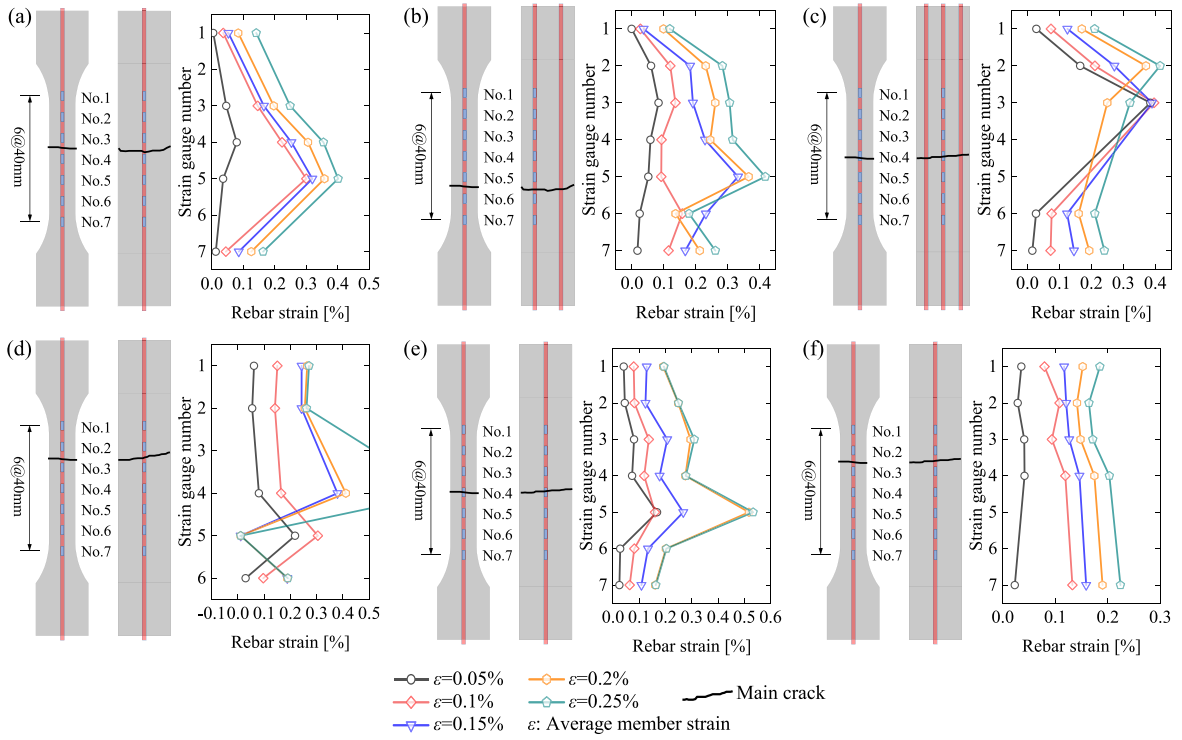

Fig. 9. Rebar strain distribution of R-CA-UHPC members: (a) d_s10; (b) $2d_s10$; (c) $3d_s10$; (d) d_s12; (e) d_s14; (f) d_s16.

Table 6
Distinctive loads and strains of R-CA-UHPC members.

Rebar	ρ_s	No.	First cracking				Yielding			Peak	
			P_{cr} [kN]	$P_{cr,The}$ [kN]	ε_{cr} [× 10^{-6}]	$\varepsilon_{cr,The}$ [× 10^{-6}]	P_y [kN]	$P_{y,The}$ [kN]	ε_y [× 10^{-6}]	P_m [kN]	ε_m [× 10^{-6}]
d_s10	1.6 %	SN-1	29.31	40.90	110	151	50.73	70.12	2438	67.10	5128
		SN-2	28.35		113		55.91			70.60	4105
		Mean	28.83		111		53.32			68.85	4616
		COV	2 %	–	2 %	–	7 %	–	–	4 %	16 %
$2d_s10$	3.2 %	SN-1	21.62	42.66	95	151	108.77	107.94	2438	116.25	2903
		SN-2	28.35		100		103.63			109.13	2730
		Mean	24.98		98		106.20			112.69	2816
		COV	19 %	–	4 %	–	3 %	–	–	4 %	4 %
$3d_s10$	5.0 %	SN-2	22.85	44.41	90	151	120.68	145.76	2438	159.80	3310
d_s12	2.3 %	SN-1	28.90	41.63	120	151	68.68	84.92	2382	75.32	2990
		SN-2	24.99		100		66.57			77.89	3085
		Mean	26.95		110		67.62			76.60	3027
		COV	10 %	–	13 %	–	2 %	–	–	2 %	2 %
d_s14	3.2 %	SN-1	24.93	42.42	85	151	67.26	94.77	2104	85.30	3103
		SN-2	26.45		78		86.27			86.47	2140
		Mean	25.69		81		76.77			85.89	2621
		COV	4 %	–	7 %	–	18 %	–	–	1 %	26 %
d_s16	4.2 %	SN-1	18.88	43.87	73	151	84.79	114.21	1958	104.93	2818
		SN-2	18.42		84		96.69			99.21	3969
		Mean	18.65		78		90.74			102.07	3393
		COV	2 %	–	11 %	–	9 %	–	–	4 %	24 %

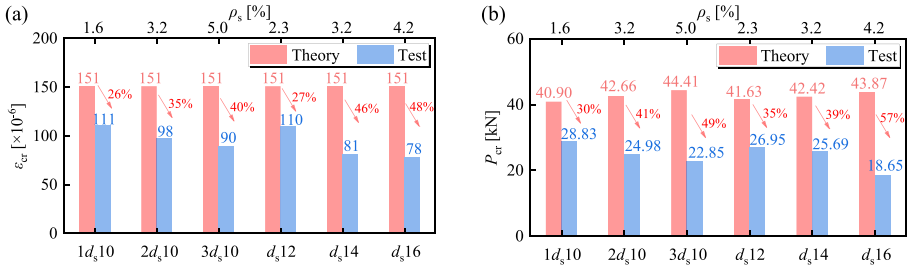

Fig. 10. Comparison between theoretical and experimental first cracking values: (a) strains; (b) loads.

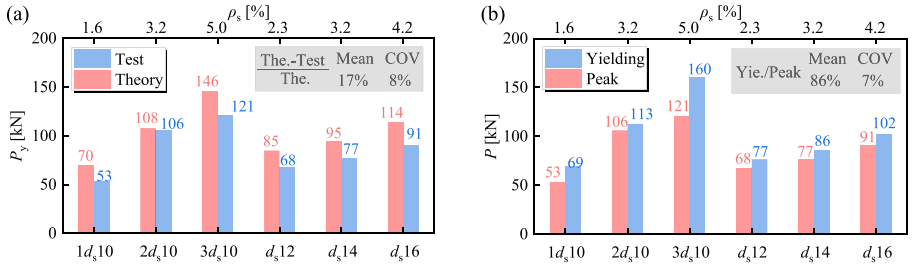

Fig. 11. Comparison of distinctive load values: (a) theoretical and experimental yielding loads; (b) experimental yielding and peak loads.

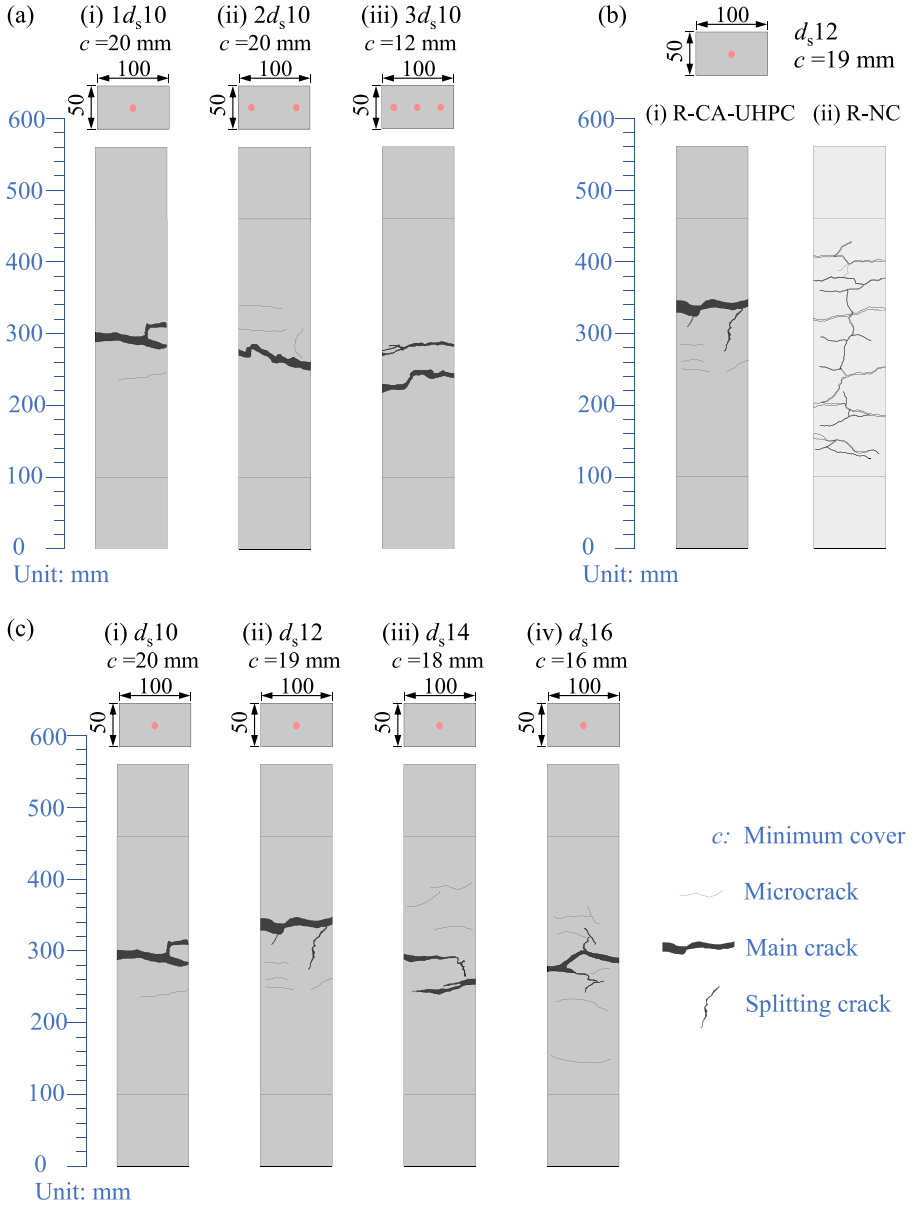

Fig. 12. Crack distribution of reinforced concrete members with different parameters: (a) rebar quantity; (b) concrete types; (c) rebar diameter.

saturated transverse cracks which were connected by the splitting cracks. By comparison, crack localization was observed at the post-yielding stage for all the R-CA-UHPC specimens, while no pronounced splitting crack was developed. This indicates that strain or crack localization is more prone to happen in R-CA-UHPC members, which is against previous knowledge that R–UHPC members has an advantage over R–NC members in achieving ductility because of the more excellent residual tensile capacity of UHPC by adding steel fibers.

The crack localization of R-CA-UHPC members is attributed to the axial tensile characteristics of CA-UHPC material, which exhibits cracking localization at the tensile strain of 2500$\mu\varepsilon$, as shown in Fig. 4. After rebar yields (the yielding strain is close to 2500$\mu\varepsilon$), fiber

debonding from the CA-UHPC matrix becomes the main tension bearing mechanism, leading to the intensified crack localization.

Moreover, as the reinforcement ratio increases, the crack localization of R-CA-UHPC members has not been significantly alleviated. According to Hung et al.'s research [22], the enhanced bond strength between rebar and UHPC due to the inclusion of steel fibers transformed the failure pattern of the R–UHPC from multiple localized cracks (no steel fibers) into a single localized crack (adding steel fibers), which will lead to the premature failure of R–UHPC reinforced with small steel rebars and subjected to monotonic loading.

The typical ultimate failure modes of R–NC and R-CA-UHPC are compared in Fig. 13. The concrete part of the R–NC member was divided into sub-components by transverse and longitudinal cracks due to the limited tensile strength of NC and bond strength between rebar and concrete. By comparison, the R-CA-UHPC member presented the fracture of the rebar at the main crack location. Qiu et al. [25] and Yu et al. [31] also demonstrated the same failure modes of R–UHPC members under axial tension. This was induced by the intensified strain concentration in the embedded rebar because of the crack localization of CA-UHPC. The significantly different failure modes of R–NC and R-CA-UHPC members demonstrate that CA-UHPC has substantially enhanced interface bond properties with rebar compared with NC.

5. Analysis of restrained shrinkage creep effect

5.1. Restrained shrinkage creep effect

Compared with the unreinforced concrete members, the free shrinkage of concrete for reinforced concrete members is restrained due to the restrained effect of rebar on concrete. This induces an initial tensile stress (also named as the restrained tensile stress $\sigma_{ct,re}$) in the concrete, that leads to a reduction in external load needed to crack the member, as well as an initial compressive stress in the rebar before the load being applied [32]. Once concrete is subjected to tension, tensile creep strain is generated due to the inherent creep behavior of concrete, which in turn reduces the shrinkage strain and restrained tensile stress of concrete. This mechanism is called stress relaxation [33]. The restrained shrinkage couples with the tensile creep, so the restrained effect on free shrinkage and the derived tensile creep effect are identified as the restrained shrinkage creep effect.

Fig. 14 plots the restrained shrinkage creep effect, where ε_{cs} is the free shrinkage strain of concrete, $\varepsilon_{cs,re}$ is the developed shrinkage of concrete under the constraint of steel bars, i.e., the restrained shrinkage strain, $\varepsilon_{ct,re}$ is the restrained tensile strain of concrete due to the restrained shrinkage creep effect, ε_{ccr} is the tensile creep strain of concrete.

Given the final state of deformation in Fig. 14, assuming that the restrained tensile stress developed in the concrete is $\sigma_{ct,re}$ and the

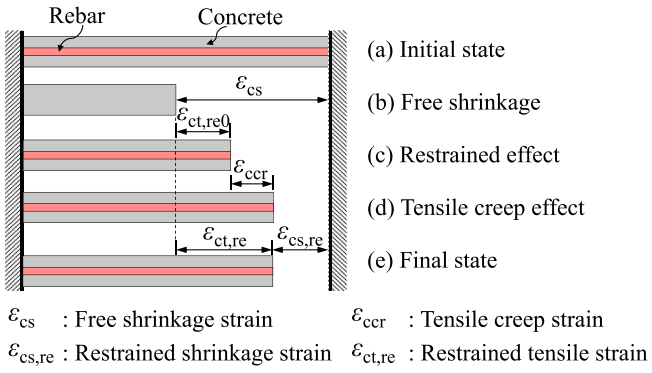

Fig. 14. Restrained shrinkage creep effect for reinforced concrete members [36].

developed restrained shrinkage strain of concrete is $\varepsilon_{cs,re}$, then the compressive strain of the rebar equals $\varepsilon_{cs,re}$ based on the assumption of deformation compatibility. According to the equilibrium of internal forces, Eq. (1) can be obtained, and then the restrained shrinkage strain $\varepsilon_{cs,re}$ is accordingly expressed in Eq. (2):

$$A_c\sigma_{ct,re} = A_sE_s\varepsilon_{cs,re} \tag{1}$$

$$\varepsilon_{cs,re} = \frac{A_c\sigma_{ct,re}}{A_sE_s} = \frac{\sigma_{ct,re}}{\rho_sE_s} \tag{2}$$

where ρ_s is reinforcement ratio, $\rho_s = A_s/A_c$, A_s is the cross-sectional area of rebar, A_c is the net cross-sectional area of concrete.

The first cracking strength f_{cr} of R-CA-UHPC can be obtained according to Eq. (3) based on the test first cracking load P_{cr} listed in Table 6.

$$P_{cr} = (1 + \alpha_E\rho_s)A_cf_{cr} \tag{3}$$

where α_E is elastic modulus ratio of rebar to CA-UHPC, $\alpha_E = E_s/E_c$; $\alpha_E\rho_s$ is axial stiffness ratio of rebar to CA-UHPC.

The induced restrained tensile stress $\sigma_{ct,re}$ in CA-UHPC for R-CA-UHPC members at the end of the curing stage can be determined as the difference between the tensile strength of CA-UHPC f_{ct} and the first cracking strength f_{cr} of R-CA-UHPC members, as expressed in Eq. (4). The obtained $\sigma_{ct,re}$ in Eq. (4) and $\varepsilon_{cs,re}$ in Eq. (2) can be considered as indirect test values.

$$\sigma_{ct,re} = f_{ct} - f_{cr} \tag{4}$$

Table 7 lists the comparison between test and theory first cracking strengths and strains for R-CA-UHPC members. The restrained tensile stress $\sigma_{ct,re}$ in CA-UHPC increases with the increasing of axial stiffness

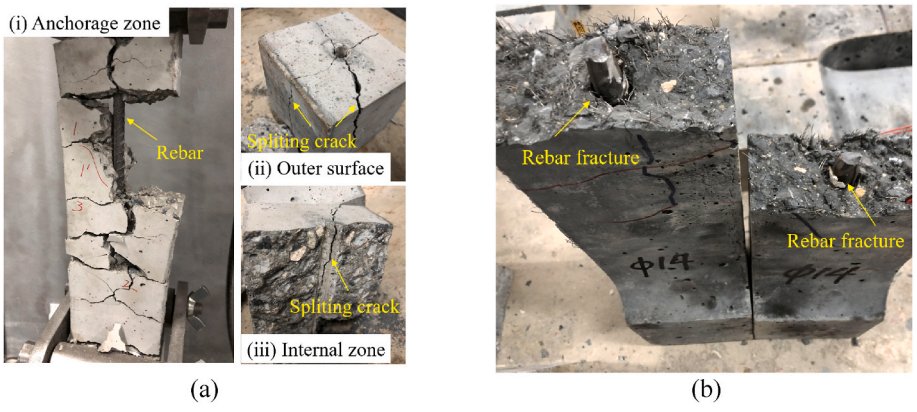

Fig. 13. Ultimate failure modes: (a) R–NC; (b) R-CA-UHPC.

Table 7
Comparison between tested and theoretical first cracking strengths and strains.

Rebar	$\alpha_E\rho_s$	Test		Theory		Restrained effect	
		f_{cr} [MPa]	ε_{cr} [$\times 10^{-6}$]	f_{ct} [MPa]	ε_{cte} [$\times 10^{-6}$]	$\sigma_{ct,re}$ [MPa]	$\varepsilon_{cs,re}$ [$\times 10^{-6}$]
d_s10	0.061	5.52	111	7.83	151	2.31	723
$2d_s10$	0.125	4.59	98			3.24	500
$3d_s10$	0.190	4.03	90			3.80	384
d_s12	0.088	5.08	110			2.75	602
d_s14	0.118	4.74	81			3.09	504
d_s16	0.167	3.33	73			4.50	517

ratio $\alpha_E\rho_s$, while the restrained shrinkage strain $\varepsilon_{cs,re}$ exhibits an opposite trend.

To further quantify the impact of the restrained shrinkage creep effect during the standard curing stage on the internal force redistribution and the first cracking of the R-CA-UHPC members, the Dischinger-differential-equation-based [37] theoretical analysis was conducted from the perspective of deformation compatibility between rebar and CA-UHPC. The first step of theoretical analysis was the quantification of three key parameters of CA-UHPC, i.e., elastic modulus, free shrinkage, and tensile creep, which are time-dependent at early age. It should be noted that owing to the relatively low water-binder ratio and the high volume use of cementitious material, the UHPC material has extremely high autogenous shrinkage but insignificant drying shrinkage [36]. Therefore, the determination of the autogenous shrinkage of CA-UHPC was performed in the following section.

5.2. Modelling of age-dependent parameters

5.2.1. Elastic modulus

This study involved the experimental measurement of the elastic modulus (100 mm × 100 mm × 300 mm prisms) for CA-UHPC at the age of 1d, 2d, 3d, 4d, 5d, 7d, 10d, 14d, 21d, and 28d under standard curing condition as stated above. The elastic modulus test results of UHPC under the same curing condition conducted by Graybeal [38] have been also collected and listed in Table 8. Based on all the data, a normalized time-dependent evolution function of elastic modulus for UHPC was developed, given in Eq. (5) and plotted in Fig. 15.

$$\frac{E_c(t)}{E_{c,28}} = 1 - e^{-19.11\left(\frac{t}{28}\right)} \tag{5}$$

where $E_{c,28}$ is the elastic modulus of UHPC at 28d, t is age in days.

5.2.2. Autogenous shrinkage

Yoo et al. [39]proposed a time-dependent model for autogenous shrinkage of UHPC, as given in Eq. (6)~ Eq. (8).

$$\varepsilon_{as}(t) = \gamma\varepsilon_{as\infty}\beta(t) \tag{6}$$

$$\varepsilon_{as\infty} = 2300e^{\left[-7.2\frac{w}{B}\right]} \tag{7}$$

Table 8
Elastic modulus of UHPC at different ages.

Reference	t [days]	$E_c(t)$ [MPa]	$E_c(t)/E_{c,28}$	t [days]	$E_c(t)$ [MPa]	$E_c(t)/E_{c,28}$
This study	1	39700	0.746	7	50500	0.949
	2	44700	0.840	10	51200	0.962
	3	47200	0.887	14	52600	0.989
	4	48900	0.919	21	52200	0.981
	5	50400	0.947	28	53200	1
Graybeal [38]	1	10500	0.251	7	39000	0.931
	2	28300	0.675	9	37600	0.897
	3	36000	0.859	28	41900	1

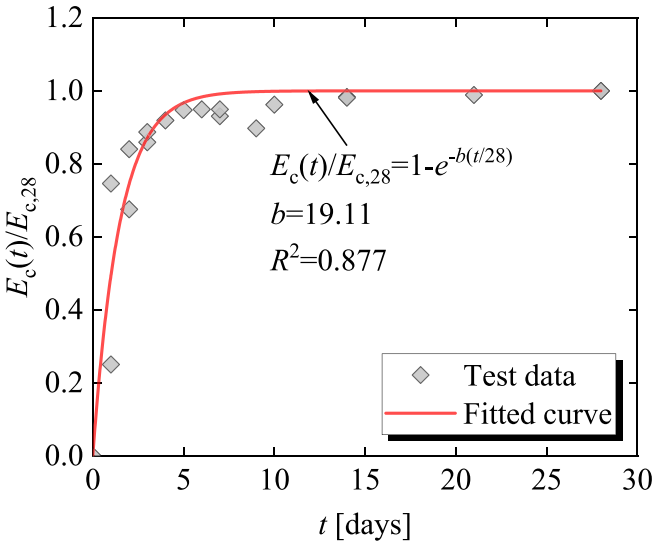

Fig. 15. Evolution of elastic modulus at early age.

$$\beta(t) = 1 - e^{\left(-0.65\sqrt{t}\right)} \tag{8}$$

where t is age in days; $\varepsilon_{as\infty}$ is the ultimate autogenous shrinkage; $\beta(t)$ is the development function of autogenous shrinkage; w/B is the water-to-binder ratio; γ is a coefficient to describe the effect of shrinkage-reducing admixture (SRA), γ is 1 when no adding SRA, while is 0.85 when including 1 % SRA.

The prediction model of autogenous shrinkage proposed by Yoo et al. is only suitable for conventional UHPC without coarse aggregate. Existing studies revealed that the addition of coarse aggregate contributed to reducing the autogenous shrinkage of the UHPC matrix. Therefore, it is essential to improve the model proposed by Yoo et al. and to extend the applicability to CA-UHPC. Li et al. [12]investigated the influence of the dosage of coarse aggregate on autogenous shrinkage of UHPC within 90d, and the test results are listed in Table 9. However, Li et al. [12]didn't develop a model that could quantify the effect of dosage of coarse aggregate on autogenous shrinkage. Based on the test data in Table 9, the mass ratio of coarse aggregate to total aggregate η (including coarse and fine aggregates) and the impact factor of coarse aggregate on autogenous shrinkage α were proposed in this study, as given in Eq. (9) and Eq. (10):

$$\eta = \frac{m_{CA}}{m_{CA} + m_{FA}} \tag{9}$$

where m_{CA} is the mass of coarse aggregate, m_{FA} is the mass of fine aggregate.

$$\alpha = \frac{\varepsilon_{as,CA-UHPC}}{\varepsilon_{as,UHPC}} \tag{10}$$

where $\varepsilon_{as,CA\text{-}UHPC}$ is the autogenous shrinkage of CA-UHPC, $\varepsilon_{as,UHPC}$ is the autogenous shrinkage of UHPC without coarse aggregate.

The relation between mass ratio η and impact factor α was fitted as plotted in Fig. 16(a) and given in Eq. (11). Therefore, the modified

Table 9
Effect of coarse aggregate on autogenous shrinkage of UHPC within 90d [12].

η	$\varepsilon_{as,CA\text{-}UHPC}$ [$\times 10^{-6}$]	$\varepsilon_{as,UHPC}$ [$\times 10^{-6}$]	α
0	615.9	615.9	1
0.125	556.9	615.9	0.904
0.225	543.5	615.9	0.882
0.325	516.7	615.9	0.839
0.425	496.7	615.9	0.806

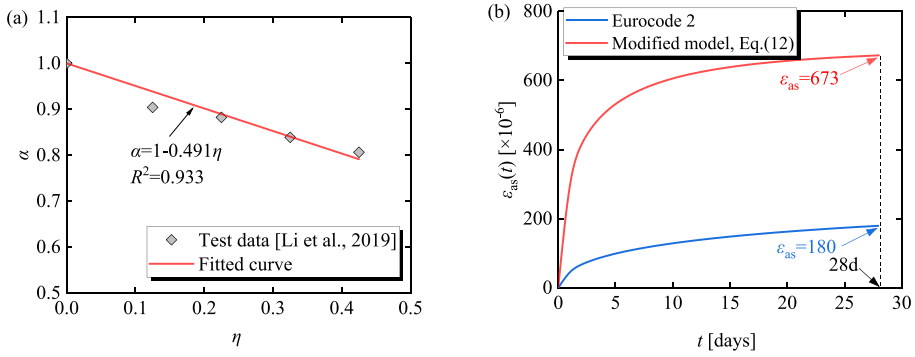

Fig. 16. Modified autogenous shrinkage model of UHPC: (a) relation between mass ratio η and impact factor α; (b) comparison with Eurocode 2.

model which was suitable for UHPC with or without coarse aggregate for describing the autogenous shrinkage development at early age was established, as expressed in Eq. (12):

$$\alpha = 1 - 0.491\eta \tag{11}$$

$$\varepsilon_{as}(t) = \gamma\alpha\varepsilon_{as\infty}\beta(t) \tag{12}$$

where α is the impact factor of coarse aggregate on autogenous shrinkage, other parameters are described shown in Eq. (6).

The w/B and mass ratio η of CA-UHPC used in this study were 0.133 and 0.433, respectively. Accordingly, the autogenous shrinkage of 673 $\mu\varepsilon$ for CA-UHPC at 28d under the standard curing was obtained according to Eq. (11) and Eq. (12) and is going to be assumed as a reference for further elaborations in this study. According to the basic material parameters of CA-UHPC used in this study, the modified autogenous shrinkage model in Eq. (12) was compared with the autogenous shrinkage model in Eurocode 2 [40], as shown in Fig.(16). Eurocode 2 significantly underestimates the autogenous shrinkage of CA-UHPC.

5.2.3. Creep

The creep here refers to the tensile creep deformation, which occurs in CA-UHPC once the interface bond between rebar and CA-UHPC comes to an effect and restrains the free shrinkage. It is difficult to accurately determine the starting time of the tensile creep. Given that there is limited research on the creep properties of UHPC currently, it is generally believed that the tensile creep coefficient is equivalent to the compressive creep coefficient for concrete [33]. The compressive creep coefficient of UHPC has been hereafter used to consider the impact of tensile creep.

The Swiss design code SIA 2052 [41] provides the evolution function of the compressive creep coefficient for UHPC as given in Eq. (13).

$$\varphi(t,t_0) = \varphi_\infty(t,t_0)\cdot\frac{(t-t_0)^a}{(t-t_0)^a + b} \tag{13}$$

where $\varphi(t,t_0)$ is the creep coefficient, $\varphi_\infty(t,t_0)$ is the final creep coefficient, t is age, t_0 is the age at first loading, a and b are coefficients as listed in Table 10.

The initial setting time of the CA-UHPC used is approximately 6~9 h, and the final setting time is 8~11 h. Therefore, the initial loading age of the tensile creep t_0 is less than 4d. Nevertheless, the Swiss design code is only suitable for t_0 equal to or larger than 4d. To derive the creep coefficient development function for t_0 earlier than 4d, the basic creep model proposed by Dischinger [37] has been used, as given in Eq. (14).

$$\varphi(t,0) = \varphi_{k0}\left(1 - e^{-\beta t}\right) \tag{14}$$

where φ_{k0} is the ultimate value of the creep coefficient, β is the coefficient of creep growth rate.

The creep coefficient from t_0 to t can be derived when using Dischinger's basic creep model [37], as expressed below:

$$\begin{aligned}\varphi(t,t_0) &= \varphi(t,0) - \varphi(t_0,0)\\ &= \varphi_{k0}e^{-\beta t_0}\left[1 - e^{-\beta(t-t_0)}\right]\\ &= \varphi_\infty(t,t_0)\left[1 - e^{-\beta(t-t_0)}\right]\end{aligned} \tag{15}$$

Consequently, the final creep coefficient $\varphi_\infty(t, t_0)$ from t_0 to t is given by:

$$\varphi_\infty(t,t_0) = \varphi_{k0}e^{-\beta t_0} \tag{16}$$

In the following section, the restrained tensile stress of CA-UHPC will be derived according to the Dischinger differential equation. The key to solving this differential equation is to assume that the development law of shrinkage is similar to that of creep. To obtain the coefficient of creep growth rate β, the time-dependent development model of autogenous shrinkage for UHPC proposed by Yoo et al. [39] was re-fitted according to the form of creep coefficient $\varphi(t,t_0)$ in Eq. (15), as given in Eq. (17):

$$\begin{aligned}\varepsilon_{as}(t) &= \varepsilon_{as\infty}\beta_{disc}(t)\\ &= \varepsilon_{as\infty}\left[1 - e^{-\beta(t-t_0)}\right]\end{aligned} \tag{17}$$

where $\beta_{disc}(t)$ is the development function of autogenous shrinkage, in which $t_0 = 0$.

The fitting result is plotted in Fig. 17. As shown, the fitted coefficient of creep growth rate β was 0.316.

Assuming $\beta = 0.316$ and $\varphi_\infty(t,t_0) = 1.2$ corresponding to $t_0 = 4$d into Eq. (16), $\Phi_{k0} = 4.25$ was obtained. Therefore, the development function of the creep coefficient corresponding to any first loading age t_0 can be given below.

$$\varphi(t,t_0) = 4.25e^{-0.316t_0}\left[1 - e^{-0.316(t-t_0)}\right] \tag{18}$$

It should be noted that investigations on the tensile creep of CA-UHPC are still lacking. Therefore, this study referred to the compressive creep model of UHPC specified in the Swiss design code SIA 2052. Furthermore, the functional form of the creep model in SIA 2052 is different from that of normal concrete provided in Eurocode 2 [40]. This study provides an initial insight into the tensile creep behavior of UHPC owing to the lack of enough experimental data. Further studies on the tensile creep mechanism as well as the tensile creep model of CA-UHPC will be continued, and the developed model will further be used to modify the following theoretical analysis.

Table 10
Final creep coefficient and coefficients a and b [41].

t_0 [days]	Curing	$\varphi_\infty(t, t_0)$	a	b
4	20 °C	1.2	0.6	3.2
7	20 °C	1.0	0.6	4.5
28	20 °C	0.9	0.6	10
–	Thermal treatment - 2 days at 90 °C and steamed	0.3	0.6	10

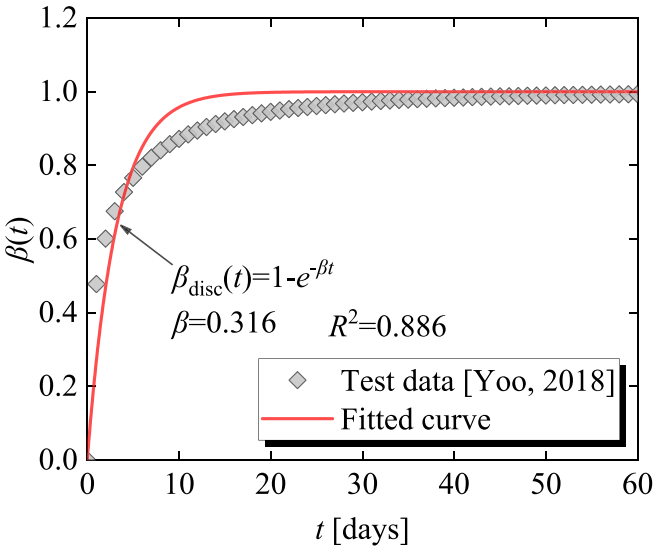

Fig. 17. Dischinger-form based time-dependent development function of autogenous shrinkage for UHPC.

5.3. Dischinger-differential-equation-based theoretical analysis

5.3.1. Theoretical derivation

For reinforced concrete members, the deformation between rebar and concrete is assumed equal through interfacial bonding force, and the strain increment of the two components at the bonding point is consistent [37]. According to deformation compatibility, the rebar and concrete are first regarded as free bodies that are separated from each other, and only constrained by interaction forces along the axis of the rebar.

Let $F_s(t,\ t_0)$ represent the interaction force between rebar and concrete during the period from the initial interaction age t_0 to t, ε_{c1} and ε_{s1} denote the elastic strain of the concrete-free body generated at the location of the rebar, and the elastic strain generated at the rebar-free body when $F_s(t,\ t_0) = 1$, respectively. As a simplification, the elastic modulus of concrete E_c is assumed to be constant. Therefore, ε_{c1} and ε_{s1} can be expressed respectively as:

$$\varepsilon_{c1} = \frac{1}{E_c A_c} \tag{19}$$

$$\varepsilon_{s1} = \frac{1}{E_s A_s} \tag{20}$$

Make:

$$\varepsilon_{11} = \varepsilon_{c1} + \varepsilon_{s1} \tag{21}$$

$$\alpha = \frac{\varepsilon_{c1}}{\varepsilon_{11}} \tag{22}$$

According to the differential equation solved by Dischinger [37], the compatibility condition for strain increment between rebar and concrete in time interval dt is:

$$dF_s(t,t_0)\varepsilon_{11} + F_s(t,t_0)\varepsilon_{c1}d\varphi(t,t_0) - d\varepsilon_{cs}(t,t_0) = 0 \tag{23}$$

where $dF_s(t,\ t_0)\varepsilon_{11}$ is the increment of elastic strain generated by the increment of interactive force, $F_s(t,\ t_0)\varepsilon_{c1}d\varphi(t,\ t_0)$ is the strain increment caused by tensile creep under interactive force, $d\varepsilon_{cs}(t,\ t_0)$ is the strain increment caused by shrinkage.

It is assumed that the development law of shrinkage is the same as that of creep, that is, the development functions of shrinkage and creep adopt Eq. (17) and Eq. (18), respectively, then:

$$d\varepsilon_{cs}(t,t_0) = \frac{\varepsilon_{cs\infty}}{\varphi_\infty} d\varphi(t,t_0) \tag{24}$$

Substituting Eq. (22) and Eq. (24) into Eq. (23) yields:

$$dF_s(t,t_0)\varepsilon_{11} + \alpha\varepsilon_{11}F_s(t,t_0)d\varphi(t,t_0) - \frac{\varepsilon_{cs\infty}}{\varphi_\infty} d\varphi(t,t_0) = 0 \tag{25}$$

The following differential equation is obtained when Eq. (25) is divided by ε_{11}:

$$dF_s(t,t_0) + \alpha d\varphi(t,t_0)F_s(t,t_0) = \frac{\varepsilon_{cs\infty}}{\varepsilon_{11}\varphi_\infty} d\varphi(t,t_0) \tag{26}$$

Solving this differential equation yields:

$$F_s(t,t_0) = \frac{\varepsilon_{cs\infty}}{\alpha\varepsilon_{11}\varphi_\infty} + Ce^{-\alpha\varphi(t,t_0)} \tag{27}$$

According to the boundary conditions, $\varphi(t,\ t_0) = 0$, $F_s(t,\ t_0) = 0$ when $t = t_0$, the integral constant C can be obtained as following:

$$C = -\frac{\varepsilon_{cs\infty}}{\alpha\varepsilon_{11}\varphi_\infty} \tag{28}$$

Substituting Eq. (28) into Eq. (27) gives:

$$F_s(t,t_0) = \frac{\varepsilon_{cs\infty}}{\alpha\varepsilon_{11}\varphi_\infty}\left[1 - e^{-\alpha\varphi(t,t_0)}\right] \tag{29}$$

Substituting Eq. (22) into Eq. (29) gives:

$$F_s(t,t_0) = \frac{\varepsilon_{cs\infty}}{\varepsilon_{c1}\varphi_\infty}\left[1 - e^{-\alpha\varphi(t,t_0)}\right] \tag{30}$$

Substituting Eq. (19) into Eq. (30) gives:

$$F_s(t,t_0) = \frac{\varepsilon_{cs\infty}}{\varphi_\infty} E_c A_c\left[1 - e^{-\alpha\varphi(t,t_0)}\right] \tag{31}$$

Therefore, the restrained tensile stress $\sigma_{ct,re}(t,\ t_0)$ due to the restrained shrinkage and inclusive of creep/relaxation effect from t_0 to t is expressed as:

$$\sigma_{ct,re}(t,t_0) = \frac{F_s(t,t_0)}{A_c} = \frac{\varepsilon_{cs\infty}}{\varphi_\infty} E_c\left[1 - e^{-\alpha\varphi(t,t_0)}\right] \tag{32}$$

The corresponding restrained shrinkage strain $\varepsilon_{cs,re}(t,\ t_0)$ is obtained by substituting Eq.(32) into Eq.(2):

$$\varepsilon_{cs,re}(t,t_0) = \frac{F_s(t,t_0)}{A_c} = \frac{\varepsilon_{cs\infty}}{\varphi_\infty}\frac{E_c}{\rho_s E_s}\left[1 - e^{-\alpha\varphi(t,t_0)}\right] \tag{33}$$

It should be noted that the restrained tensile stress $\sigma_{ct,re}(28,\ t_0)$ and the restrained shrinkage strain $\varepsilon_{cs,re}(28,\ t_0)$ for R-CA-UHPC members under standard curing for 28d are simplified as $\sigma_{ct,re,28}$ and $\varepsilon_{cs,re,28}$, respectively. Besides, the two results obtained based on Dischinger's differential equation are marked as analytical values.

5.3.2. Quantification of uncertain parameters

The determination of E_c and t_0 needs to be discussed to obtain the accurate values of $\sigma_{ct,re,28}$ and $\varepsilon_{cs,re,28}$ according to Eq. (32) and Eq. (33). On the one hand, the elastic modulus of CA-UHPC develops with time at the curing stage. On the other hand, the initial time t_0 (also named as the initial loading age) for the interaction between rebar and CA-UHPC, which also governs the magnitude of the tensile creep coefficient $\varphi(t,\ t_0)$, is difficult to determine at the curing stage.

For the quantification of E_c, the concept of equivalent average elastic modulus $E_{c,eq}$ at the early age from t_0 to t was proposed, as shown in Fig. 18(a) and Eq. (34), the changing elastic modulus $E_c(t)$ was equivalent to a constant elastic modulus $E_{c,eq}$ by making area S_{FABCG} equal to S_{FDEG}. Based on this method, the initial interactive time t_0 also determined the magnitude of $E_{c,eq}$.

$$E_{c,eq} = \frac{\int_{t_0}^{t} E_c(t)dt}{t - t_0} \tag{34}$$

The initial setting time of CA-UHPC is approximately 6~9 h, and the

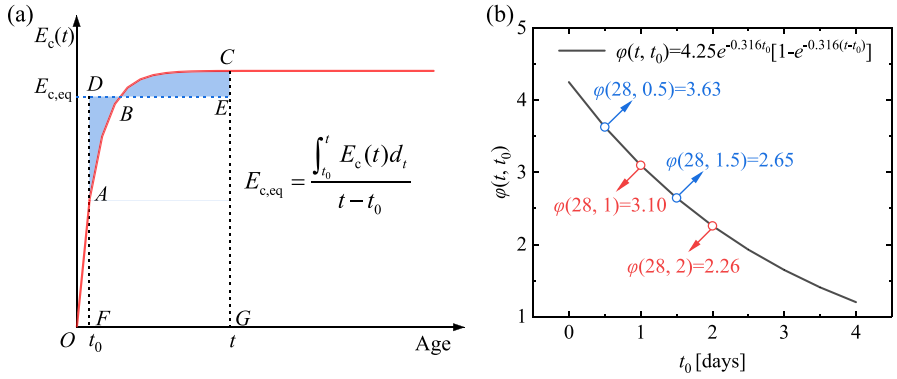

Fig. 18. Quantification of uncertain parameters: (a) equivalent average elastic modulus; (b) influence of initial loading age on tensile creep coefficient.

final setting time is approximately 8~11 h. Therefore, it can be preliminarily considered that the initial interactive time t_0 was 0.5d.

The analysis of the influence of E_c and t_0 on $\sigma_{ct,re,28}$ and $\varepsilon_{cs,re,28}$ will be conducted based on two cases. Case I: when $E_c = E_{c,eq}$, t_0 was taken as 0.5d, 1.0d, 1.5d, and 2.0d, respectively (the corresponding influence of t_0 on tensile creep coefficient is shown in Fig. 18(b)). Case II : when t_0 = 0.5d , E_c was taken as $0.4E_{c,eq}$, $0.6E_{c,eq}$, $0.8E_{c,eq}$, and $E_{c,eq}$, respectively. The influence of E_c and t_0 on the analytical values of $\sigma_{ct,re,28}$ and $\varepsilon_{cs,re,28}$ under these two cases, and the comparison between the analytical and test values are shown in Fig. 19.

As shown in Fig. 19(a), when $E_c = E_{c,eq}$, the analytically calculated values of $\sigma_{ct,re,28}$ and $\varepsilon_{cs,re,28}$ increased with the initial interaction time t_0, with an amplification from 4 % to 12 %. As shown in Fig. 19(b), when t_0 = 0.5d, the analytically calculated values of $\sigma_{ct,re,28}$ and $\varepsilon_{cs,re,28}$ increased with E_c, with an amplification from 24 % to 61 %. It can be concluded that the value of E_c has a more significant impact on the calculated values of $\sigma_{ct,re,28}$ and $\varepsilon_{cs,re,28}$ compared to that of t_0. Taking into account the difference between the analytical and test values comprehensively, the analytical values of $\sigma_{ct,re,28}$ and $\varepsilon_{cs,re,28}$ corresponding to $E_c = E_{c,eq}$ and $t_0 = 0.5$d were chosen to further compare with the test values, as shown in Fig. 20.

As plotted, the mean value and coefficient of variation of the ratio of analytical value to test value for the restrained tensile stress were 0.96 and 13 %, and the corresponding items for the restrained shrinkage strain were 0.96 and 12 %. It demonstrates the applicability and the high accuracy of the Dischinger-differential-equation-based analytical solution and the related quantification of time-dependent parameters, including elastic modulus $E_c(t)$, autogenous shrinkage $\varepsilon_{as}(t)$, tensile creep coefficient $\varphi(t,t_0)$, equivalent average elastic modulus $E_{c,eq}$ and the initial interactive time t_0, and could be used to predict the restrained tensile stress $\sigma_{ct,re,28}$ and the restrained shrinkage strain $\varepsilon_{cs,re,28}$ of R-CA-UHPC members under the standard curing condition.

5.3.3. *Simplified prediction model*

The analytical values of the restrained tensile stress and the restrained shrinkage strain at different ages when $t_0 = 0.5$d and $E_c = E_{c,eq}$, are shown in Tables 11 and 12, respectively. The fitted development functions of the restrained tensile stress and the restrained shrinkage strain at early age are shown in Fig. 21, and given in Eq. (35) and Eq. (36), respectively. It is obvious that the two items have the same development function. According to the development function of the restrained tensile stress, the cracking risk of R-CA-UHPC members at early age can be evaluated once mastering the development function of the tensile strength for CA-UHPC.

$$\frac{\sigma_{ct,re}(t)}{\sigma_{ct,re,28}} = 1 - e^{-7.25\left(\frac{t}{28}\right)} \tag{35}$$

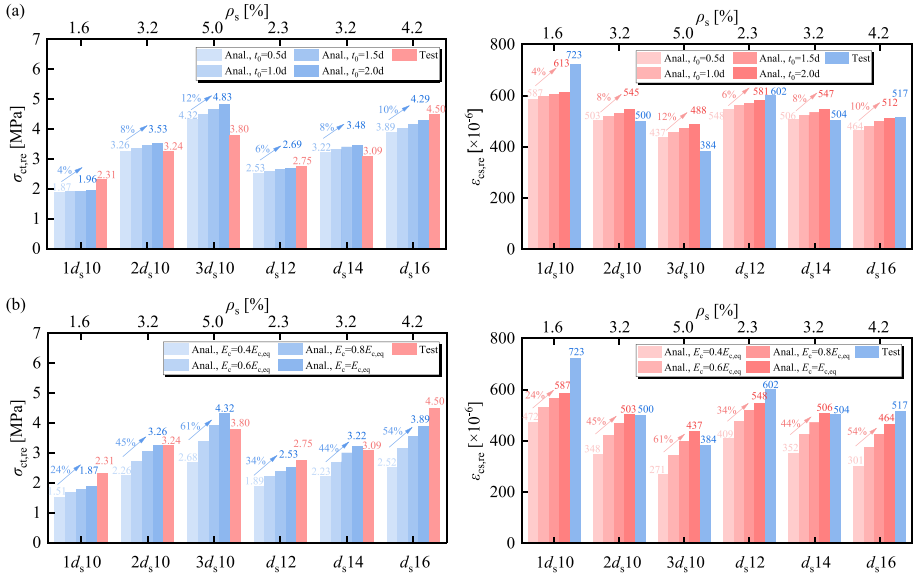

Fig. 19. Influence of elastic modulus and initial loading age on restrained tensile stress and restrained shrinkage strain: (a) $E_c = E_{c,eq}$, varying t_0; (b) t_0 = 0.5d, varying E_c.

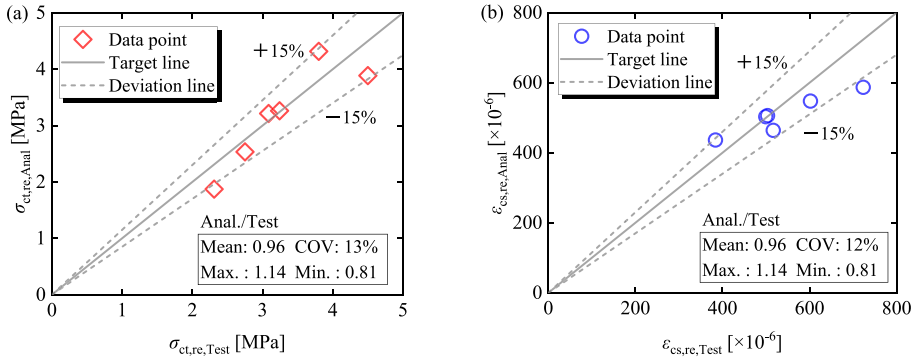

Fig. 20. Comparison between analytical and test values of CA-UHPC: (a) restrained tensile stress; (b) restrained shrinkage strain.

Table 11
Analytical values of $\sigma_{ct,re}(t)$ at different ages when $t_0 = 0.5$d and $E_c = E_{c,eq}$.

Rebar	t	$\sigma_{ct,re}(t)$	$\sigma_{ct,re}(t)/\sigma_{ct,re,28}$	Rebar	t	$\sigma_{ct,re}(t)$	$\sigma_{ct,re}(t)/\sigma_{ct,re,28}$
	[days]	[MPa]	–		[days]	[MPa]	–
d_s10	1	0.27	0.14	2d_s10	1	0.47	0.14
	2	0.70	0.38		2	1.23	0.38
	3	1.02	0.54		3	1.78	0.54
	4	1.25	0.67		4	2.17	0.66
	5	1.41	0.75		5	2.45	0.75
	7	1.62	0.87		7	2.81	0.86
	14	1.84	0.98		14	3.19	0.98
	21	1.87	1.00		21	3.25	1.00
	28	1.87	1.00		28	3.26	1.00
3d_s10	1	0.62	0.14	d_s12	1	0.37	0.14
	2	1.63	0.38		2	0.95	0.38
	3	2.35	0.54		3	1.38	0.54
	4	2.87	0.66		4	1.69	0.67
	5	3.24	0.75		5	1.91	0.75
	7	3.70	0.86		7	2.19	0.86
	14	4.20	0.97		14	2.48	0.98
	21	4.29	0.99		21	2.52	1.00
	28	4.32	1.00		28	2.53	1.00
d_s14	1	0.46	0.14	d_s16	1	0.56	0.14
	2	1.21	0.38		2	1.47	0.38
	3	1.75	0.54		3	2.12	0.54
	4	2.14	0.66		4	2.58	0.66
	5	2.42	0.75		5	2.92	0.75
	7	2.77	0.86		7	3.34	0.86
	14	3.14	0.98		14	3.79	0.98
	21	3.20	1.00		21	3.87	0.99
	28	3.22	1.00		28	3.89	1.00

Table 12
Analytical values of $\varepsilon_{cs,re}(t)$ at different ages when $t_0 = 0.5$d and $E_c = E_{c,eq}$.

Rebar	t	$\varepsilon_{cs,re}(t)$	$\varepsilon_{cs,re}(t)/\varepsilon_{cs,re,28}$	Rebar	t	$\varepsilon_{cs,re}(t)$	$\varepsilon_{cs,re}(t)/\varepsilon_{cs,re,28}$
	[days]	[× 10^{-6}]	–		[days]	[× 10^{-6}]	–
d_s10	1	85	0.14	2d_s10	1	73	0.14
	2	221	0.38		2	189	0.38
	3	320	0.54		3	274	0.54
	4	391	0.67		4	334	0.66
	5	443	0.75		5	378	0.75
	7	508	0.87		7	433	0.86
	14	576	0.98		14	492	0.98
	21	585	1.00		21	501	1.00
	28	587	1.00		28	503	1.00
3d_s10	1	63	0.14	d_s12	1	79	0.14
	2	165	0.38		2	206	0.38
	3	238	0.54		3	298	0.54
	4	290	0.66		4	364	0.67
	5	327	0.75		5	412	0.75
	7	374	0.86		7	473	0.86
	14	425	0.97		14	536	0.98
	21	434	0.99		21	545	1.00
	28	437	1.00		28	548	1.00
d_s14	1	73	0.14	d_s16	1	67	0.14
	2	191	0.38		2	175	0.38
	3	275	0.54		3	253	0.54
	4	336	0.66		4	308	0.66
	5	380	0.75		5	348	0.75
	7	436	0.86		7	399	0.86
	14	495	0.98		14	452	0.98
	21	504	1.00		21	461	0.99
	28	506	1.00		28	464	1.00

$$\frac{\varepsilon_{cs,re}(t)}{\varepsilon_{cs,re,28}} = 1 - e^{-7.25\left(\frac{t}{28}\right)} \tag{36}$$

The restraint degree ζ, defined as the ratio of the restrained tensile stress $\sigma_{ct,re}$ (analytical values) to the tensile strength f_{ct} at 28d under the standard curing condition, was proposed to characterize the degree to which the rebar contributed to reducing the first cracking strength for CA-UHPC. Similarly, the free degree ψ, expressed as the ratio of the restrained shrinkage strain $\varepsilon_{cs,re}$ (analytical values) to the free shrinkage strain $\varepsilon_{cs,re}$ at 28d under the standard curing condition, was defined to quantify the effect of rebar on the free shrinkage development of CA-UHPC. The expressions of ζ and ψ are given in Eq. (37) and Eq. (38), respectively, and the calculated values are listed in Table 13.

$$\zeta = \frac{\sigma_{ct,re}}{f_{ct}} \tag{37}$$

$$\psi = \frac{\varepsilon_{cs,re}}{\varepsilon_{cs}} \tag{38}$$

The restraint degree ζ and free degree ψ are highly correlated with the axial stiffness ratio $\alpha_E\rho_s$ (E_sA_s/E_cA_c) of rebar to concrete. The relation between ζ, ψ and $\alpha_E\rho_s$ were linearly fitted, plotted in Fig. 22, with a goodness-of-fit R^2 of up to 97 %. The fitted expressions are given in Eq. (39) and Eq. (40), respectively. It is worth noting that the applicable conditions of these expressions are: (1) steel rebar reinforced CA-UHPC members under standard curing for 28 days, and (2) corresponding reinforcement ratio $0<\rho_s \leq 5$ %.

$$\zeta = 0.045 + 2.83\alpha_E\rho_s \tag{39}$$

$$\psi = 0.973 - 1.91\alpha_E\rho_s \tag{40}$$

Therefore, the first cracking strength f_{cr} and strain ε_{cr} of R-CA-UHPC members under the standard curing for 28 days can be predicted based on the restraint degree ζ as follows, once obtaining the tensile strength f_{ct}, the elastic modulus E_c, and the axial stiffness ratio of rebar to CA-UHPC $\alpha_E\rho_s$.

$$f_{cr} = f_{ct}(1-\zeta) \tag{41}$$

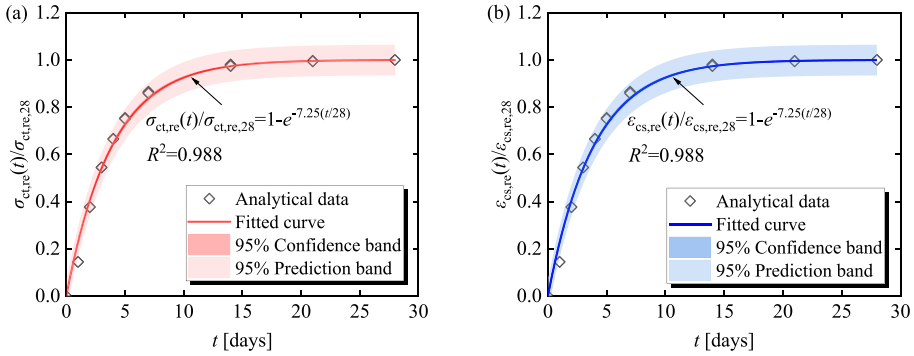

Fig. 21. Time-dependent evolution functions of: (a) restrained tensile stress; (b) restrained shrinkage strain.

Table 13
Restraint degree ζ and free degree ψ of R-CA-UHPC members.

Rebar	$\alpha_E\rho_s$	Tensile stress			Shrinkage strain		
		$\sigma_{ct,re}$ [MPa]	f_{ct} [MPa]	ζ	$\varepsilon_{cs,re}$ [× 10^{-6}]	ε_{cs} [× 10^{-6}]	ψ
d_s10	0.061	2.31	7.83	0.24	587	695	0.87
$2d_s10$	0.125	3.24		0.42	503		0.72
$3d_s10$	0.190	3.80		0.55	437		0.63
d_s12	0.088	2.75		0.32	548		0.79
d_s14	0.118	3.09		0.41	506		0.73
d_s16	0.167	4.50		0.50	464		0.67

$$\varepsilon_{cr}=\frac{f_{cr}}{E_c} \tag{42}$$

As described in sec.4.3, the restrained shrinkage creep effect postponed rebar yielding by inducing pre-compressive strain $\varepsilon_{cs,re}$ (equal to the restrained shrinkage strain) and stress $E_s\varepsilon_{cr,re}$ in the rebar. The pre-compressive strain $\varepsilon_{cs,re}$ could be predicted according to Eq. (38) and Eq. (40). The actual rebar strain at the average member strain ε reaching ε_{sy} was obtained by subtracting $\varepsilon_{cs,re}$ from ε_{sy}, as given in Eq. (43).

$$\varepsilon_{y1}=\varepsilon_{my,s}=\varepsilon_{sy}-\varepsilon_{cs,re}=\varepsilon_{sy}-\psi\varepsilon_{cs} \tag{43}$$

The counterpart CA-UHPC strain at the average member strain ε reaching ε_{sy} can be expressed as the sum of restrained tensile strain $\varepsilon_{ct,re}$ and ε_{sy}, as expressed in Eq. (44):

$$\varepsilon_{my,c}=\varepsilon_{sy}+\varepsilon_{ct,re}=\varepsilon_{sy}+\frac{\sigma_{ct,re}}{E_c} \tag{44}$$

where the restrained tensile stress $\sigma_{ct,re}$ can be predicted according to Eq. (37) and Eq. (39)

Therefore, the apparent yielding load (as the average member strain reaching ε_{sy}) could be calculated in Eq. (45).

$$P_y=P_{my,c}+P_{my,s}=A_c\sigma_{ct}(\varepsilon=\varepsilon_{my,c})+A_s\sigma_s(\varepsilon=\varepsilon_{my,s}) \tag{45}$$

where the tensile stress-strain relations of CA-UHPC and rebar are referred to Figs. 4 and 5, respectively.

Fig. 23 plots the comparison between prediction and test values for the first cracking strength f_{cr}, the first cracking strain ε_{cr}, and the yielding load P_y. As shown, the prediction values were 1.04, 0.97, and 1.03 times the test values for f_{cr}, ε_{cr}, and P_y, respectively, and the corresponding coefficient of variation were 12 %, 16 %, and 8 %, respectively. It indicated that the models established had a high accuracy exceeding 90 % and could be used to predict these characteristic responses for R-CA-UHPC members.

5.4. Structural design suggestions

In general, the tensile capacity of NC elements is neglected in R–NC structures because of the limited tensile strength of NC material. UHPC and CA-UHPC present significantly improved tensile strength through the enhanced dense microstructures and the addition of steel fibers, which is promising for more resilient structures. The tensile behavior of R-CA-UHPC members is not just a simple superposition of the tensile properties of steel bars and CA-UHPC, but the relatively high shrinkage of CA-UHPC and the interaction between rebar and CA-UHPC must be considered in structural design to ensure the safety at the serviceability limit state as well as the ultimate limit state.

The influence of the restrained shrinkage and related creep-induced stress relaxation effects on the tensile stress development of CA-UHPC and the tensile strain development of rebar for the R-CA-UHPC members are plotted in Fig. 24. As shown, the restrained tensile stress for CA-UHPC developed at the curing stage accounts for a considerable proportion of the tensile strength of CA-UHPC material, causing the premature cracking of the member at service stage. The development function of the restrained tensile stress at the curing stage is suggested

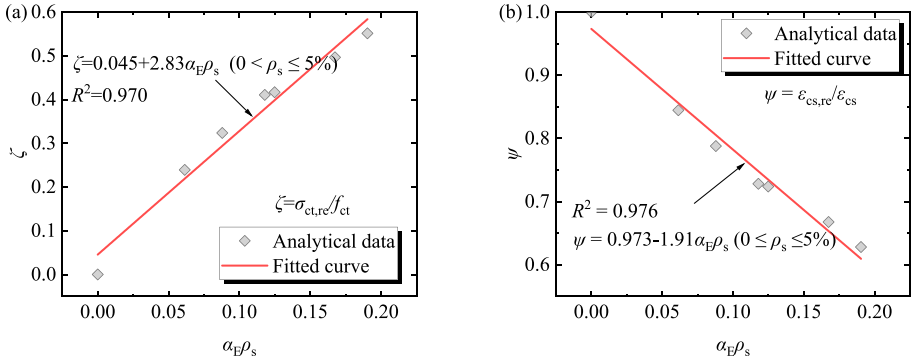

Fig. 22. Relation between axial tension stiffness ratio $\alpha_E\rho_s$ and (a) restraint degree ζ; (b) free degree ψ.

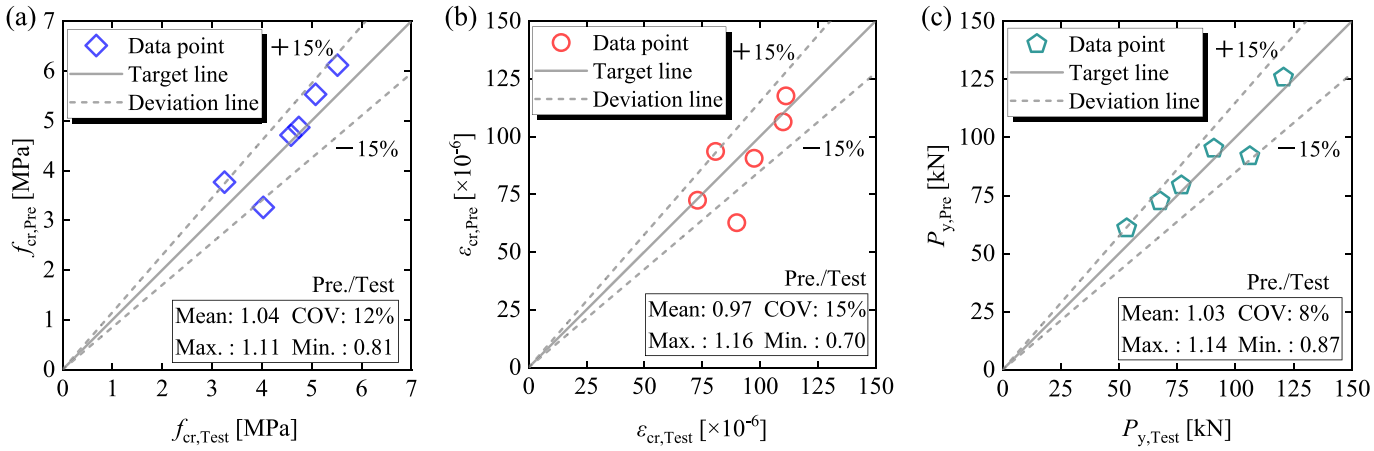

Fig. 23. Comparison between prediction and test values: (a) first cracking strength f_{cr}; (b) first cracking strain ε_{cr}; (c) yielding load P_y.

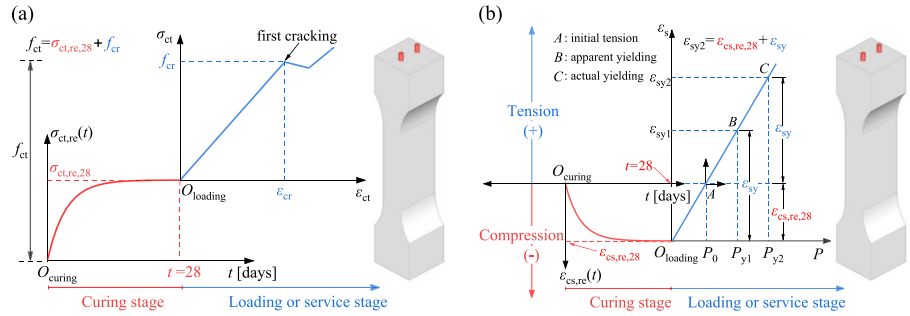

Fig. 24. Stress and strain development of R-CA-UHPC members at different stages: (a) tensile stress of CA-UHPC; (b) rebar strain.

using Eq. (35), and the resulting first cracking values are suggested to predict according to Eq. (39)~(42).

As shown in Fig. 24(b), the interaction between rebar and concrete leads to pre-compression in the rebar at the curing stage. The evolution of the compressive strain due to the restrained shrinkage, can be quantified based on Eq. (36). At the service stage under the tensile load, the rebar firstly sustains compression and has to zero the compression until reaching point A and starts bearing tension. Point B, marked as the apparent yielding point, is determined by the average member strain reaching the yielding strain of rebar ε_{sy}, while the actual strain of rebar merely arrives ε_{sy}-$\varepsilon_{cr,re,28}$. By comparison, point C is the actual yielding point for the rebar, where the average member strain and the rebar strain are ε_{sy}+$\varepsilon_{cr,re,28}$ and ε_{sy}, respectively. The final compressive strain or the restrained shrinkage strain $\varepsilon_{cr,re,28}$ is recommended to be predicted according to Eq. (38) and Eq. (40). Accordingly, the corresponding apparent yielding and actual-yielding loads for R-CA-UHPC members are to be determined based on the superposition of the tensile loads carried by CA-UHPC and rebar, respectively.

6. Conclusions

Based on the above investigations, the main conclusions are:

(1) The axial tensile response of R–NC members consists of the linear-elastic phase, the stabilized cracking phase, and the yielding phase accompanied by the longitudinal splitting cracking. The axial tensile response of R-CA-UHPC members is decomposed into the linear-elastic, the stabilized multi-cracking, the rebar yielding (localized cracking in CA-UHPC), and fracture phases. The excellent bond properties between rebar and CA-UHPC prevent the emergence of splitting cracks, but intensify the crack localization for CA-UHPC and strain concentration for rebar, leading to the ultimate fracture of rebar.

(2) The restrained shrinkage creep effect at the curing stage induces a restrained tensile stress in CA-UHPC and a restrained shrinkage compressive strain in rebar, which reduces the first cracking of CA-UHPC and delays the yield of rebar. The restrained tensile stress increases with the increase of the axial stiffness ratio of rebar to CA-UHPC, while the restrained shrinkage strain exhibits an opposite trend.

(3) Based on the test results of this study and literature, the development model of elastic modulus for CA-UHPC at early age has been developed. The development models of autogenous shrinkage and tensile creep for CA-UHPC at early age have been established in the light of data from the literature. Based on these age-dependent models, the restrained tensile stress and shrinkage strain have been quantified according to Dischinger's differential equation, and have demonstrated a high accuracy of up to 96 % by comparing with the test results.

(4) The concepts of restraint degree and free degree were proposed and fitted with the axial stiffness ratio of rebar to CA-UHPC, to determine the restrained effect of rebar on free shrinkage of CA-UHPC. On this basis, prediction models of the first cracking stresses, the first cracking strains, and the yielding loads for R-CA-UHPC members under axial tension were established with a prediction accuracy of exceeding 90 %.

CRediT authorship contribution statement

Zhanchong Shi: Writing – review & editing, Writing – original draft, Project administration, Methodology, Investigation, Formal analysis, Conceptualization. **Minfei Liang:** Writing – review & editing, Formal

analysis. **Qingtian Su:** Writing – review & editing, Supervision, Methodology, Funding acquisition, Conceptualization. **Terje Kanstad:** Writing – review & editing, Supervision. **Liberato Ferrara:** Writing – review & editing, Supervision.

Declaration of competing interest

The authors declare that they have no known competing financial interests or personal relationships that could have appeared to influence the work reported in this paper.

Data availability

Data will be made available on request.

Acknowledgements

The financial support provided by Fujian Transportation Science and Technology Project (Grant NO. 202126) is greatly appreciated by the authors. The first author also acknowledges the financial support of the China Scholarship Council (Grant NO. 202006260216).

References

[1] B. Graybeal, E. Brühwiler, B.-S. Kim, F. Toutlemonde, Y.L. Voo, A. Zaghi, International perspective on UHPC in bridge engineering, J. Bridge Eng. 25 (2020) 04020094.
[2] K. Habel, E. Denarié, E. Brühwiler, Experimental investigation of composite ultra-high-performance fiber-reinforced concrete and conventional concrete members, ACI Struct. J. 104 (2007) 93.
[3] H. Martín-Sanz, B. Herraiz, E. Brühwiler, E. Chatzi, Shear-bending failure modeling of concrete ribbed slabs strengthened with UHPFRC, Eng. Struct. 222 (2020) 110846.
[4] Y. Zhang, X. Li, Y. Zhu, X. Shao, Experimental study on flexural behavior of damaged reinforced concrete (RC) beam strengthened by toughness-improved ultra-high performance concrete (UHPC) layer, Compos. B Eng. 186 (2020) 107834.
[5] Y. Zhang, Y. Zhu, M. Yeseta, D. Meng, X. Shao, Q. Dang, G. Chen, Flexural behaviors and capacity prediction on damaged reinforcement concrete (RC) bridge deck strengthened by ultra-high performance concrete (UHPC) layer, Construct. Build. Mater. 215 (2019) 347–359.
[6] P. Buitelaar, R. Braam, N. Kaptijn, Reinforced high performance concrete overlay system for rehabilitation and strengthening of orthotropic steel bridge decks, in: 2004 Orthotropic Bridge Conference, 2004.
[7] J. Cao, X. Shao, Z. Zhang, H. Zhao, Retrofit of an orthotropic steel deck with compact reinforced reactive powder concrete, Structure and Infrastructure Engineering 12 (2016) 411–429, https://doi.org/10.1080/15732479.2015.1019894.
[8] S. Wang, Z. Ke, Y. Gao, Y. Zhang, Long-term in situ performance investigation of orthotropic steel bridge deck strengthened by SPS and RPC solutions, J. Bridge Eng. 24 (2019) 04019054, https://doi.org/10.1061/(ASCE)BE.1943-5592.0001421.
[9] D. Wang, C. Shi, Z. Wu, J. Xiao, Z. Huang, Z. Fang, A review on ultra high performance concrete: Part II. Hydration, microstructure and properties, Construct. Build. Mater. 96 (2015) 368–377.
[10] L. Yang, C. Shi, Z. Wu, Mitigation techniques for autogenous shrinkage of ultra-high-performance concrete–A review, Compos. B Eng. 178 (2019) 107456.
[11] J. Liu, F. Han, G. Cui, Q. Zhang, J. Lv, L. Zhang, Z. Yang, Combined effect of coarse aggregate and fiber on tensile behavior of ultra-high performance concrete, Construct. Build. Mater. 121 (2016) 310–318, https://doi.org/10.1016/j.conbuildmat.2016.05.039.
[12] C. Li, B. Chen, J. Wei, Shrinkage and mechanical properties of UHPC with coarse aggregate, J. Traffic Transport. Eng. 19 (2019) 11–20.
[13] Z. Shi, Q. Su, F. Kavoura, M. Veljkovic, Uniaxial tensile response and tensile constitutive model of ultra-high performance concrete containing coarse aggregate (CA-UHPC), Cement Concr. Compos. 136 (2023) 104878, https://doi.org/10.1016/j.cemconcomp.2022.104878.
[14] L. Li, L. Xu, Y. Zeng, K. Cui, Y. Chi, L. Huang, Understanding the role of coarse aggregate on tensile fatigue behaviors of ultra-high performance concrete, Cement Concr. Compos. 139 (2023) 105069.
[15] J. Cheng, Study on Flexural Fatigue Performance of Ultra High Performance Concrete with Coarse Aggregate, Master's Dissertation, Southeast University, 2018.
[16] J. Qi, Y. Bao, J. Wang, L. Li, W. Li, Flexural behavior of an innovative dovetail UHPC joint in composite bridges under negative bending moment, Eng. Struct. 200 (2019) 109716.
[17] Z. Liu, M. Alsomiri, M. Li, X. Chen, J. Meng, Experimental investigation on the flexural behavior of coarse aggregate reactive powder concrete (CA-RPC) bridge deck, Eng. Struct. 271 (2022) 114951.
[18] Y. Wang, X. Shao, J. Cao, Experimental study on basic performances of reinforced UHPC bridge deck with coarse aggregates, J. Bridge Eng. 24 (2019) 04019119.
[19] K. Lu, Q. Xu, L. Du, J. Wang, Y. Yao, Fatigue performance of prefabricated coarse aggregate ultrahigh-performance concrete deck subjected to negative bending moment, Eng. Struct. 274 (2023) 115098.
[20] J. Jungwirth, A. Muttoni, Structural Behavior of Tension Members in UHPC, École Polytechnique Fédérale de Lausanne, 2004. IS-Beton.
[21] T. Makita, E. Brühwiler, Tensile fatigue behaviour of ultra-high performance fibre reinforced concrete combined with steel rebars (R-UHPFRC), Int. J. Fatig. 59 (2014) 145–152.
[22] C.-C. Hung, H.-S. Lee, S.N. Chan, Tension-stiffening effect in steel-reinforced UHPC composites: constitutive model and effects of steel fibers, loading patterns, and rebar sizes, Compos. B Eng. 158 (2019) 269–278, https://doi.org/10.1016/j.compositesb.2018.09.091.
[23] H. Yuan, Theoretical Analysis and Experimental Research on Tensile Performance of Reinforced Reactive Powder Concrete, Doctoral Thesis, Beijing Jiaotong University, 2009.
[24] Z. Zhang, X.-D. Shao, P. Zhu, Direct tensile behaviors of steel-bar reinforced ultra-high performance fiber reinforced concrete: effects of steel fibers and steel rebars, Construct. Build. Mater. 243 (2020) 118054.
[25] M. Qiu, Y. Zhang, S. Qu, Y. Zhu, X. Shao, Effect of reinforcement ratio, fiber orientation, and fiber chemical treatment on the direct tension behavior of rebar-reinforced UHPC, Construct. Build. Mater. 256 (2020) 119311, https://doi.org/10.1016/j.conbuildmat.2020.119311.
[26] C. Bian, J.-Y. Wang, Mechanical and damage mechanisms of reinforced ultra high performance concrete under tensile loading, Construct. Build. Mater. 226 (2019) 259–279, https://doi.org/10.1016/j.conbuildmat.2019.07.162.
[27] J.-Y. Guo, J.-Y. Wang, C. Bian, Synergistic tensile response of reinforced ultra high performance concrete with low fiber contents, Case Stud. Constr. Mater. 17 (2022) e01629.
[28] C. Bian, J. Guo, J. Wang, J. Xiao, Nominal tensile strength reduction and its mechanism of ultra-high performance concrete with steel bar reinforcements, J. Build. Eng. 65 (2023) 105778.
[29] M. Roy, C. Hollmann, K. Wille, Influence of fiber volume fraction and fiber orientation on the uniaxial tensile behavior of rebar-reinforced ultra-high performance concrete, Fibers 7 (2019) 67.
[30] M. Khorami, J. Navarro-Gregori, P. Serna, Tensile behaviour of reinforced UHPFRC elements under serviceability conditions, Mater. Struct. 54 (2021) 1–17.
[31] J. Yu, T. Shi, J. Yu, Z. Xie, K. Yu, Experimental study of tensile properties of composite system of high performance concrete and reinforcements, J. Tongji Univ. Nat. Sci. 49 (2021) 825–833.
[32] K. Fields, P.H. Bischoff, Tension stiffening and cracking of high-strength reinforced concrete tension members, ACI Struct. J. 101 (2004) 447–456.
[33] S.A. Altoubat, D.A. Lange, Creep, shrinkage, and cracking of restrained concrete at early age, ACI Mater. J. 98 (2001) 323–331.
[34] Dalian University of Technology, Standard Test Methods for Fiber Reinforced Concrete, China Planning Press, Beijing, China, 2010.
[35] SAC/TC183, GB / T228-2002 Metallic Materials-Tensile Testing at Ambient Temperature, General Administration of Quality Supervision, Inspection and Quarantine of the People's Republic of China, 2002. Beijing, China.
[36] D.-Y. Yoo, N. Banthia, Y.-S. Yoon, Effectiveness of shrinkage-reducing admixture in reducing autogenous shrinkage stress of ultra-high-performance fiber-reinforced concrete, Cement Concr. Compos. 64 (2015) 27–36.
[37] H. Rüsch, D. Jungwirth, H.K. Hilsdorf, Creep and Shrinkage: Their Effect on the Behavior of Concrete Structures, Springer-Verlag, New York, U.S.A., 2012.
[38] B.A. Graybeal, Compressive behavior of ultra-high-performance fiber-reinforced concrete, ACI Mater. J. 104 (2007) 146–152, https://doi.org/10.14359/18577.
[39] D.-Y. Yoo, S. Kim, M.-J. Kim, Comparative shrinkage behavior of ultra-high-performance fiber-reinforced concrete under ambient and heat curing conditions, Construct. Build. Mater. 162 (2018) 406–419, https://doi.org/10.1016/j.conbuildmat.2017.12.029.
[40] European Committee for Standardization, EN 1992-1-1: Eurocode 2: Design of Concrete Structures - Part 1-1, General rules and rules for buildings, Brussels, Belgium, 2004.
[41] Sia, SIA 2052 Recommendation: Ultra-High Performance Fibre Reinforced Cement-based Composites (UHPFRC) Construction material, dimensioning und application, Zurich, Switzerland, 2016.